Geophys. J. Int. (2007) **170,** 275–298 doi: 10.1111/j.1365-246X.2007.03393.x

Application of stacking and inversion techniques to three-dimensional wide-angle reflection and refraction seismic data of the Eastern Alps

Michael Behm,[1] Ewald Brückl,[1] Werner Chwatal[1] and Hans Thybo[2]

[1] *Institute of Geodesy and Geophysics, Vienna University of Technology, Gusshausstrasse* 27-29/1282, 1040 *Vienna, Austria. E-mail: mbehm@mail.tuwien.ac.at*

[2] *Geological Institute, University of Copenhagen, Øster Voldgade* 10, DK-1350 *Copenhagen K, Denmark*

Accepted 2007 February 7. Received 2007 February 5; in original form 2006 January 3

SUMMARY

We present new methods for the interpretation of 3-D seismic wide-angle reflection and refraction data with application to data acquired during the experiments CELEBRATION, 2000 and ALP 2002 in the area of the Eastern Alps and their transition to the surrounding tectonic provinces (Bohemian Massif, Carpathians, Pannonian domain, Dinarides). Data was acquired on a net of arbitrarily oriented seismic lines by simultaneous recording on all lines of seismic waves from the shots, which allows 2-D and 3-D interpretations. Much (80%) of the data set consists of crossline traces. Low signal to noise (S/N) ratio in the area of the young orogens decreases the quality of travel time picks. In these seismically heterogeneous areas it is difficult to assign clearly defined arrivals to the seismic phases, in particular on crossline record sections.

In order to enhance the S/N ratio, signal detection and stacking techniques have been applied to enhance the *Pg*-, *Pn*- and *PmP* phases. Further, inversion methods have been developed for the interpretation of WAR/R-data, based on automated 1-D inversion (*Pg*) and the application of the delay time concept (*Pn*). The results include a 3-D velocity model of the crust based on *Pg* waves, time and depth maps of the Moho and a *Pn*-velocity map. The models based on stacked data are robust and provide a larger coverage, than models based on travel time picks from single-fold (unstacked) traces, but have relatively low resolution, especially near the surface. They were used as the basis for constructing models with improved resolution by the inversion of picks from single-fold data. The results correlate well with geological structures and show new prominent features in the Eastern Alps area and their surrounds. The velocity distribution in the crust has strong lateral variations and the Moho in the investigation area appears to be fragmented into three parts.

Key words: continental crust, controlled-source seismology, Eastern Alps, Moho discontinuity, seismic processing, seismic structure.

1 INTRODUCTION

From 1997 to 2003, a new generation of 3-D wide-angle reflection and refraction (WAR/R) experiments to study the structure of the lithosphere was applied in Central Europe (Gutercb *et al*. 2003a). The field geometries of these experiments were characterized by a net of arbitrarily oriented seismic lines along which a large number of mobile seismographs simultaneously recorded seismic waves from all shots. A main advantage of this field concept is that both 2-D and 3-D interpretation can be carried out in order to enhance the coverage of structures in the area of concern.

Traditional methods for the interpretation of WAR/R seismic data include first arrival diving wave tomography (Hole 1992; Zelt & Barton, 1998), tomographic inversion of travel times of refracted and reflected waves (Zelt and Smith 1992; Zelt *et al.* 1999; Hobro *et al.* 2003; Bleibinhaus & Gebrande 2006), and forward modelling of reflections and refractions by ray tracing (Červený & Psencik 1984). Travel time picks for these interpretations are usually based on phase correlation in (single-fold) record sections and are necessary requirements for the application of these methods. Therefore low S/N ratio in the seismic data restricts the applicability, in particular for tomographic inversion. Often low S/N ratio occurs in orogens, such as the Alps, due to the scattering of seismic energy by the complex tectonic structures. Further, restrictions to charge size and the number of shot holes of the seismic sources due to economic or environmental reasons contribute to low S/N ratio, which increases the uncertainty of the travel time picks, and thereby decreases the ray coverage of the area under study.

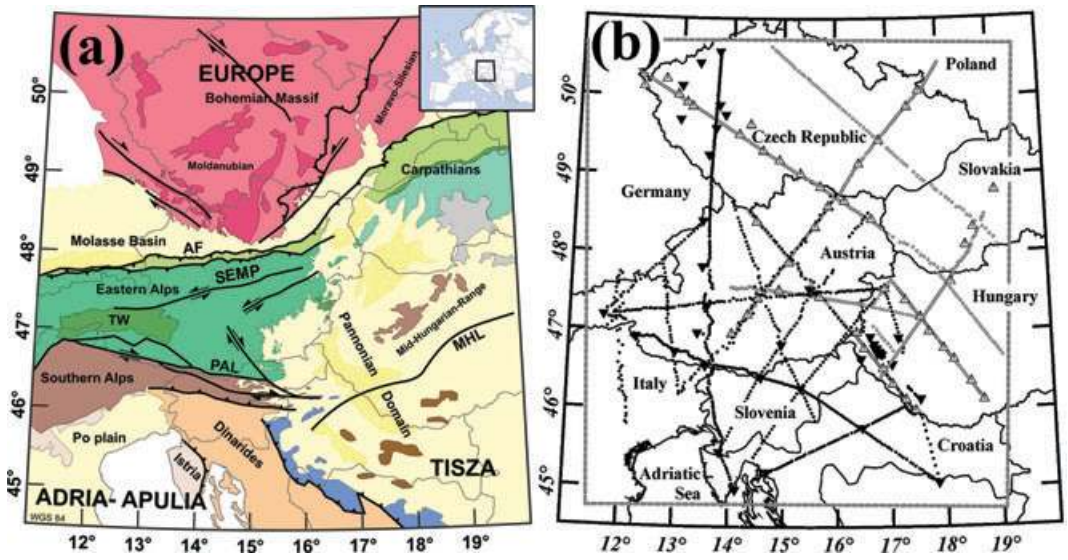

Figure 1. (a) Tectonic setting of the investigation area. (AF: Alpine Front; PAL: Periadriatic Lineament; MHL, Mid Hungarian Line; TW: Tauern Window; SEMP: Salzach-Ennstal-Mürz-Puchberg-Line). (b) Geometry of the seismic profiles in the investigation area: Black circles and inverted triangles represent receivers and shots from ALP 2002; grey circles and triangles represent receivers and shots from the 3rd deployment of CELEBRATION 2000.

Stacking is a method to reduce the problems caused by low S/N ratio. Stacking of the traces for several shots aims to suppress random and signal generated noise. Stacking techniques are widely used in exploration seismology. The benefits of stacking global broadband seismograms and lithospheric refraction and wide-angle reflection data in the time-offset domain have been demonstrated by Astiz *et al.* (1996) and Richard-Dinger & Shearer (1997).

In this paper we apply signal detection and stacking to WAR/R data from recent lithospheric projects (CELEBRATION 2000; ALP 2002) and present inversion methods for the stacked data. We derive a robust 3-D model by stacking techniques and refine it by traditional methods, which rely on travel time picks from record sections. Because only 20 percent of the data is recorded on inline stations, a large amount of information is present in the crossline record sections. However, due to the low S/N ratio in some regions and complex seismic structure in the investigated area, reliable crossline phase correlations were difficult to make in the record sections. The stacking techniques simplify the wave field and enhance the arrivals of the seismic phases and therefore, a larger amount of the 3-D data set could be incorporated than with only travel times from the record sections. The resulting models are robust, have large coverage and are finally enhanced in the details by use of traditional methods, wherever accurate travel time picks are available from the record sections.

Sections 2 and 3 target the tectonic setting and seismic exploration of the Eastern Alps and describe the data set as well. In Section 4 we outline the methods used for stacking and inversion of stacked data for three types of waves (*Pg*, *Pn*, *PmP*) and show the results. In Section 5 we compare the models obtained from inverting stacked data to results derived by traditional methods based on travel time tomography. The results from both methods are merged such that one final, preferred velocity model of the crust and uppermost mantle and a final representation of the Moho topography in the time domain are derived. Structural interpretation, migration and depth conversion lead to the Moho depth map (Section 6). As we use many models and some nonstandard abbreviations throughout this paper, a glossary is given in appendix A.

This paper focuses on the stacking and inversion methods, their differences to traditional methods and the new seismic models of the Eastern Alps. Although the final seismic models of the area are derived by a combination of stacking and traditional approaches (Behm, 2006), we keep the descriptions of the traditional methods and the combination of methods to a minimum. The stacking methods and the new seismic models of the Eastern Alps are the central issues of the paper, whereas an in-depth tectonic-geological interpretation will later be presented in connection with interpretation of the 2-D profiles.

2 TECTONIC SETTING & SEISMIC EXPLORATION OF THE EASTERN ALPS

The investigation area covers the eastern half of the Eastern Alps and their surrounding tectonic provinces (Fig. 1a). These provinces are the Bohemian Massif and the Molasse basins to the north, the Carpathians to the northeast, the Pannonian basin to the east, the Dinarides to the southeast, as well as Istria and the Po-Plain to south. The Eastern Alps continue into the Western Alps further to the west.

From Mesozoic times to present the tectonic evolution of the investigation area has been dominated by the Alpine-Carpathian-Dinaridic orogenesis, which was initiated during the opening of the Atlantic in the early Jurassic and the subsequent collision between Africa and Europe (e.g. Schmid *et al.* 2004). The Alpine evolution is complex, involving several stages, and has been better investigated in the western parts of the orogen than the eastern segment. The main tectonic units are the Bohemian promontory, the Adriatic-Apulian plate and the Tisza Block. In a regional context, the Eastern Alps are located between the Bohemian Massif, the Carpathians, the Pannonian domain, the Southern Alps and the Dinarides. Apart from the Variscan Bohemian Massif, all these units formed during the Alpine orogeny.

The Bohemian Massif consists of the highly metamorphosed Moldanubian crystalline crust in the west and the less metamorphosed crystalline Moravo-Silesian crust in the east. The Molasse

basins represent the northern foreland of the Alps and Carpathians and are filled with Tertiary sediments.

The Eastern Alps mainly comprise the Austroalpine nappe stack, which consists of the Paleozoic crystalline basement and several Mesozoic cover sequences. These nappes are interrupted by Penninic windows, of which the most prominent is the Tauern Window where the sub-Penninic granite gneiss of the European basement has been exhumed. The Periadriatic Line (PAL) defines the transition from the Austroalpine to the Southern Alps. The Dinarides have a diffuse boundary to the Southern Alps (Doglioni & Bosselini 1987). The peninsula Istria represents the southern foreland, and as the Dinarides, it is mainly covered by the thick Adriatic carbonate platform.

The Vienna and Pannonian basins formed contemporary during roll back of the southwestward Carpathian subduction and tectonic escape of the Eastern Alps in the Miocene (Ratschbacher, 1991). The Pannonian Basin is interrupted by the Transdanubian mountain range. The Mid-Hungarian Line is a WSW-ENE striking zone, which represents the transition from the northern part of the Pannonian Basin to the Tisza block (or micro-plate) (Tomljenovic & Csontos 2001). Neogene deposits cover most of the Tisza block.

Earthquake seismology brought the first data on the deep structure of the crust in the Eastern Alps. The crust-mantle boundary (Moho) was discovered by A. Mohorovičić (1910) based on recordings of the Kulpa Valley earthquake (8.10.1909). The evaluation of the Tauern (28.11.1923) and Schwadorf (8.10.1927) earthquakes by V. Conrad gave further knowledge about the crust in the area by suggesting a layered structure of the crystalline crust.

The exploration of the Eastern Alps by WAR/R experiments started with refraction lines around the Eschenlohe quarry (southern Germany) some 40 yr ago. Seismic lines radiated from this shot point over the Alps to the shot points Lago Lagorai and Trieste (Giese *et al.* 1976). The projects ALP 75, SUD-ALP and ALP 78 supplied further refraction and wide-angle reflection lines (Yan & Mechie, 1989; Scarascia & Cassinis, 1997). In former Czechoslovakia WAR/R experiments were carried out on several international profiles (Beranek & Zounkova, 1979; Mayerova *et al.* 1994) and the deep seismic reflection profiles 3T and 8HR cross our investigation area (Tomek 1993). The Pannonian Basin in Hungary was explored by deep reflection seismic profiling during the Pannonian Geotraverse (Posgay *et al.* 1996). Crustal structures indicating extensional processes of the Pannonian basin were described by Hajnal *et al.* (1996). In former Yugoslavia nine deep seismic refraction/wide-angle reflection profiles were recorded during the years 1964–1983 (Dragašević *et al.* 1990). Two of them are in our investigation area and extend in a SW-NE direction from the Adriatic Sea across the Dinarides to the Panonnian basin (Joksović & Andrić, 1983; Skoko *et al.* 1987). Dèzes & Ziegler (2001) compiled a Moho map of Europe. The most recent results in the area of the Bohemian promontory and the transition to the Carpathians arise from the CELEBRATION 2000 project (Hrubcová *et al.* 2005). The TRANSALP project has provided a transect of the western part of the Eastern Alps between Munich and Verona integrating WAR/R, deep seismic reflection and passive seismic monitoring data. It reveals the Moho structure and a large crustal S-dipping ramp (Lüschen *et al.* 2004; Bleibinhaus & Gebrande 2006). Deep seismic reflection profiles in NE Styria have provided data on the structure of the Rechnitz Penninic window (Grassl *et al.* 2004). However, the combination of the 2-D results of the above experiments to a 3-D image of the Eastern Alpine crust and upper lithosphere is not unique and cannot answer fundamental questions about the structure and tectonic evolution of the area like the direction of subduction or implications of the tectonic escape of the Eastern Alps.

3 DATA

We present interpretation of seismic data from an area of 600 × 660 km (W-E × N-S; Fig. 1b). From the 3rd deployment of the CELEBRATION 2000 project, we use recordings of seismic waves from 55 shots on 844 receivers deployed along 7 profiles, with a total length of approximately 2800 km. The corresponding figures for the ALP 2002 project are 39 shots, 947 receivers, 4300 km profile length and 13 profiles. Overall, 7 profiles of 20 have a sufficient shot- and receiver density for 2-D interpretations. The average receiver distance is 2.9 km ('high density profiles' with a total of 1208 receivers) and 5.8 km ('low density profiles' with a total of 583 receivers). Shot charges were on average 300 Kg, which provide a maximum observable offset of 200 km (*Pg*) and of 400 km (*Pn*), depending on the local situation. The whole data set comprises 78933 traces, of which about 20 percent are inline data. Detailed descriptions of these two experiments are given by Guterch *et al.* (2001), Guterch *et al.* (2003b) and Brückl *et al.* (2003).

In all Sections, 9831 *Pg* picks and 2940 *Pn* picks were correlated (Fig. 2), including picks (*Pg*: 232, *Pn*: 83) from earlier investigations (e.g. Alpine Explosion Seismology Group, Reporter H. Miller, 1976). Record sections with high S/N ratio were obtained from shots and receivers in the Bohemian Massif and in the Pannonian Basin, whereas the S/N ratio is much lower in the Alpine area.

Despite that *PmP* waves are well recognizable in many records, their exact arrival time is difficult to pick. In particular on crossline gathers, the close grouping of *Pg*, *Pn* and PmP made it difficult to attribute specific phases to the visible arrivals. It is a general

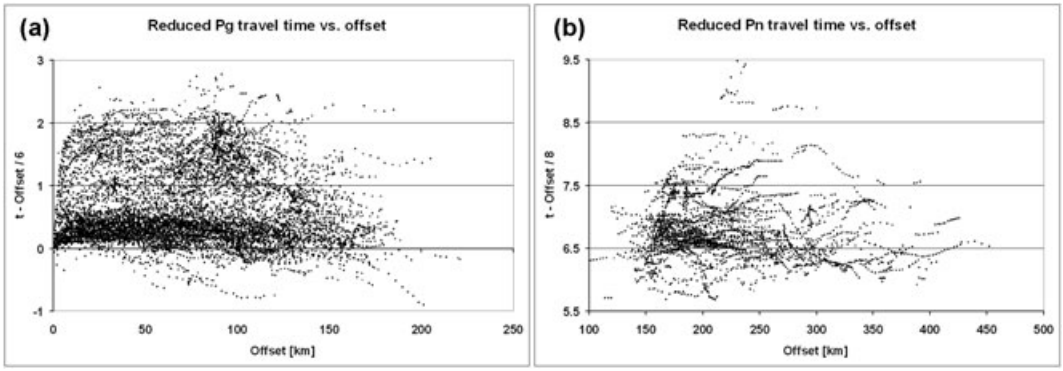

Figure 2. *Pg* (a) and *Pn* (b) picks from the original shot gathers, reduced with 6 km s^{-1} (a) and 8 kms^{-1} (b).

problem to the interpretation of cross-line recordings that a large part of the prominent arrivals is found between the critical offset and the *Pn* cross-over distance, where *Pg*, *Pn* and *PmP* overlap or are very close. Therefore we did not include *PmP* picks, since only few arrivals could be identified with sufficient accuracy and the selected inversion routines focus on *Pg* and *Pn* waves.

We refer to travel times obtained from the original record sections (single-fold traces) as 'record travel times', while travel times obtained from stacked data are called 'stack travel times'.

4 STACKING AND INVERSION OF STACKED DATA

Signal detection, stacking and inversion techniques are applied to the data set, which is of heterogeneous quality. We focus on three types of waves: diving waves through the upper and lower crust (*Pg*), refracted waves from the uppermost mantle (*Pn*), and wide-angle reflections (in particular *PmP*).

4.1 Geometry, sorting and binning

For global stacking of seismic data all traces form one gather (Astiz *et al.* 1996). Traces are stacked within offset bins and a 1-D velocity-depth function can be derived from stacked data. Regional studies, which aim at 3-D models of the velocity structure, demand for spatial sorting of seismic data into cells (Richards-Dinger & Shearer 1997). We also apply specific sorting routines and follow the terminology established in industrial 3-D reflection seismic surveys (e.g. Yilmaz, 2001).

The 600 – by – 660 – km (W-E – by – N-S) – sized investigation area is located between 11.5° E – 19°E and 45°N – 51°N. It is covered by a regular, quadratic grid with a predefined grid point (x, y) spacing l_G. Square cells are assigned to and centred at the grid points. The cell sizes l_C (length of the cell sides) are usually larger than l_G in order to guarantee sufficient data within one cell (Fig. 3).

The geometry of the seismic traces is defined by their source (SRC) and receiver (RCV) locations, which define the common midpoint (CMP) location and the absolute offset (*aoff*) of any trace. Trace sorting with CMP as primary key results in a *CMP-gather*. A CMP-gather contains all traces, which have their common midpoints inside a particular cell (Fig. 3a). Stacking all traces of a CMP-gather result in a *CMP-stack*. Trace sorting with either the SRC or the RCV as primary key results in a *SRC&RCV-gather* (Fig. 3b). A SRC&RCV-gather contains all traces with either their shots or their receivers inside a cell and stacking of these traces results in a *SRC&RCV-stack.* Picked travel times from the CMP- and SRC&RCV-stacks are assigned to the centre of the data in the cell. This data centre is calculated as the average of the CMP-locations, and SRC- and RCV-locations respectively, of all traces in the cell. Kriging is used to interpolate such spatially assigned travel times to arbitrary locations (e.g. grid points, SRC, RCV, CMP).

In case of *Pg* and *Pn* waves, the traces of the CMP-gather are further sorted with the absolute offset as a secondary key in order to extract velocity information. An offset bin stack (*OFB-stack*) is generated by arranging the traces in absolute offset bins with bin size l_B and subsequent stacking within each bin. A linear moveout (*LMO*) – correction with a proper reduction velocity is applied prior to stacking in order to approximately align the interesting phases (*Pg* or *Pn*) within the bins and to improve coherency. The absolute offset of the stacked traces is calculated as the average of the absolute offsets of all traces inside each bin. While a CMP- or a SRC&RCV-stack is always one trace, an OFB-stack is a collection of traces, which are arranged along their absolute offset in ascending order (Fig. 4). An OFB-stack represents the 1-D travel time curve of a cell

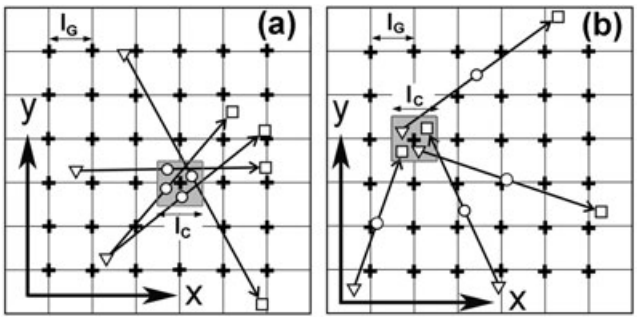

Figure 3. (a) Schematic map view of CMP-sorting. All traces, which have their CMP inside the cell belong to the CMP-gather. (b) Schematic map view of source/receiver (SRC&RCV-) sorting. All traces, which have either source or receiver inside the cell, belong to the SRC&RCV-gather. Thick crosses: grid points. Grey box: cell assigned to the grid point. Triangles: shots. Rectangles: receivers. Circles: CMP's.

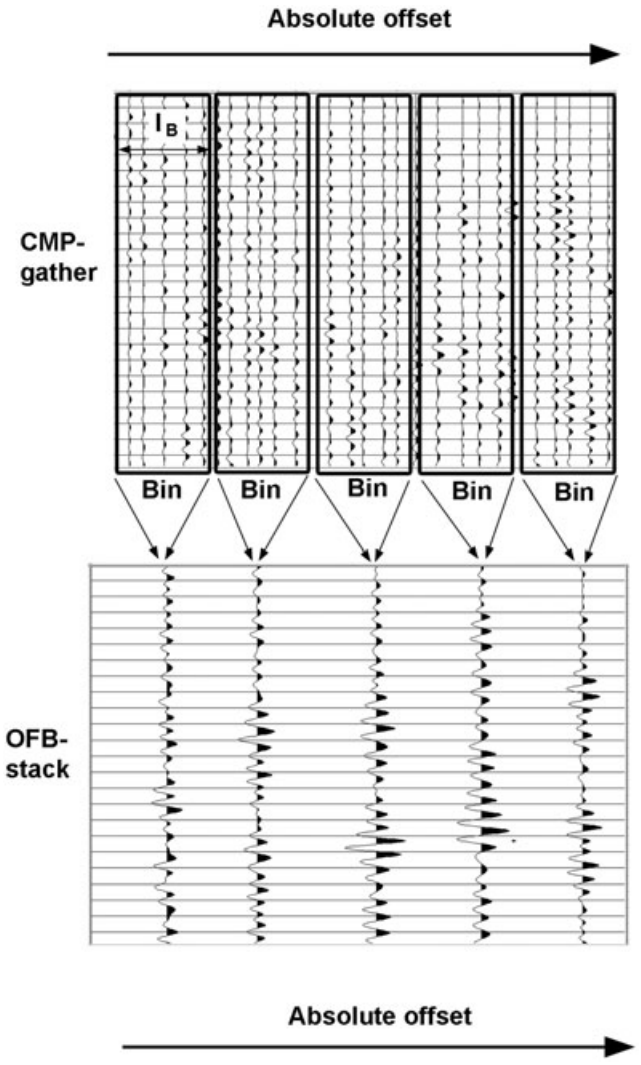

Figure 4. Creating an OFB-stack from a CMP-gather. Traces of the gather are subdivided into offset bins and are stacked after LMO and static corrections are applied. The OFB-stack is the collection of all stacked traces which are arranged in ascending order according to their absolute offset.

and therefore its velocity-depth function. Picked travel times from an OFB-stack deliver the input for velocity-depth inversions. The results of these inversions are either a 1-D velocity-depth function (*Pg*) or a constant velocity (*Pn*) of a cell. Again these results are assigned to the data centre (average of the CMP-locations of all traces in the cell) and Kriging is used to interpolate the results to the grid points or other locations.

In all cases, specific time corrections (e.g. static or dynamic corrections) are applied to the traces prior to stacking in order to enhance the stacking result.

4.2 Pre-stack signal processing and travel time picking of stacked traces

We apply trace equalization and frequency filtering (Ormsby bandpass, 2-4-12-24 Hz, minimum delay) to the data. For WAR/R data, we cannot expect to achieve constructive interference of the individual seismic phases. Therefore, prior to stacking, the seismic trace is transformed to its envelope (complex amplitude), which is always positive. This process further acts as a low-pass frequency filter. In order to enhance first arrivals of the *Pg* and *Pn* phases, we apply the *STA* (short-term average) to *LTA* (long-term average) ratio event detection techniques, similar to that proposed by Astiz *et al.* (1996). The averaging time of the envelope is 0.05 s for the *STA* and 1.00 s for the *LTA* (Fig. 5). A crucial step to improve the stacking result was to exclude traces without any signal contributions by visual inspection (trace editing).

Accurate travel time picking from stacked amplitudes (with or without the STA/LTA-algorithm applied) is not as well defined as for original waveforms due to the loss of the waveform of the original wavelet by the transformation to complex amplitudes. We pick the arrival time corresponding to the maximum amplitude gradient of stacked complex amplitudes with (*Pg* and *Pn*) or without (*PmP*) signal detection algorithms applied. This corresponds to picking the maximum of the derivative of the stacked envelope trace. Therefore, all stacked traces are low pass filtered (Ormsby bandpass: 0.01-0.05-0.1-0.5 Hz) and differentiated. Travel time picking from the first maxima of these low frequency wavelets had an uncertainty of 0.15 – 0.20 s, which is significantly larger than travel times picking from single-fold traces with high S/N ratio. This procedure introduced also a systematic shift between travel times from the stacked and the single-fold traces. As the latter time is close to the true travel time, we compensate for this systematic time shift by later calibration. Travel time picking from both stacked and record data was always made by visual inspection.

4.3 Stacking and inversion of *Pg* phases

CMP-sorting and OFB-stacking was applied to enhance *Pg*-phases and to derive a robust 3-D velocity model of the crust. Trace editing and offset limitation to 250 km reduced the number of traces to 34301. The parameters of CMP-sorting and OFB-stacking are $l_G =$ 20 km (grid spacing), $l_B = 5$ km (bin size), and LMO velocity = 6 km s^{-1}. The cell size l_C was adapted to CMP-density and was 38 km on average. To optimize the stacking results, static corrections relative to the CMP are applied prior to stacking in order to compensate for the influence of sedimentary basins. A description of the static corrections is given in Appendix B.

The coverage of the whole data set allows for stacking and inversion in 715 cells. The whole procedure, from the CMP-gather to the resulting velocity-depth function, is illustrated for two example cells in Fig. 6. The OFB-stacks are picked for smooth travel time curves for 1-D interpretation (Figs 6b and e), where small 'humps' in the travel time curves are excluded as they can result from significant deviations from the 1-D assumption and inaccurate static corrections. Shadow zones are also not picked in order to allow for possible low velocity zones. For each cell a 1-D velocity-depth function is derived at depth nodes each 1 km down to a depth of 20 km and progressively increasing at levels >20 km. (Figs 6c and f). The velocity is linearly interpolated between the depth nodes. Starting from an initial model, we invert the 1-D travel time curve iteratively for velocity (slowness) changes at the depth nodes using Truncated Singular Value Decomposition (TSVD), *cf*. Appendix C. TSVD allows determination of the resolution elements of the velocities. The resolution elements describe the reliability of each velocity (slowness) (e.g. Menke, 1984) and range between 0 (completely undetermined) and 1 (uniquely determined). The resolution elements are calculated based on the ray geometry of the final model. The velocities determined by the 1-D inversion are well constrained in layers with turning rays, such that the lower crust is generally better resolved than the middle crust because few picks are made in the middle offset range. Synthetic tests show that velocities at the maximum penetration depth are always well resolved by the 1-D inversion (Appendix C).

Finally the velocities are interpolated at the levels of the depth nodes, resulting in a 3-D velocity model $v^s{}_{Pg}(x,y,z)$ (Fig. 7, left column). Picked *Pg* record travel times from the original traces (t_{obs}; Fig. 2a) are used to check the accuracy of the model. The code by Vidale (1990) is used for the calculation of travel times t_{calc}. Neglecting shots with small charges, 9531 rays are used for the calculation of the travel time residuals $dt = t_{obs} - t_{calc}$, which have a mean error of +0.06 s and an root mean square (RMS) error of 0.328 s (Fig. 8a). There is a statistically significant offset-dependency of the residuals, which indicate that, on average, $v^s{}_{Pg}$ provides too low velocities. $v^s{}_{Pg}$ provides smoothed local velocity information because: (1) CMP-sorting, stacking in offset bins and the subsequent picking tend to smear strong lateral velocity variations, (2) exact static corrections cannot always be supplied, and (3) the uniform 20 km grid spacing may provide a too coarse sampling interval in areas of dense ray coverage. These effects are most pronounced in areas with strong surface velocity variations, e.g. in sedimentary basins. A detailed error analysis (Behm, 2006) shows that 45 percent of the variance of the residuals can be attributed to time delays of the shots. These time delays correlate with the variation of the sedimentary cover such that large delays are associated with shots located in deep basins. Assuming that these time delays result from overestimated velocities of the sediments, we find that 'sub-sedimentary' structures in $v^s{}_{Pg}$ reproduce *Pg* travel times within an RMS error of 0.21 s.

4.4 Stacking and inversion of *Pn* phases

4.4.1 Delay time modelling

Information about Moho depth and upper mantle *P*-wave velocity are derived from the analyses of *Pn* phases. Trace editing and offset limitation from 150 to 400 km reduced the number of traces to 20727. We apply stacking and inversion methods based on a delay time model (delay time decomposition). The principle of delay time modelling is illustrated in Fig. 9a (e.g. Gardner, 1939; Telford *et al.*1990). A travel time t of a wave passing a refractor can be

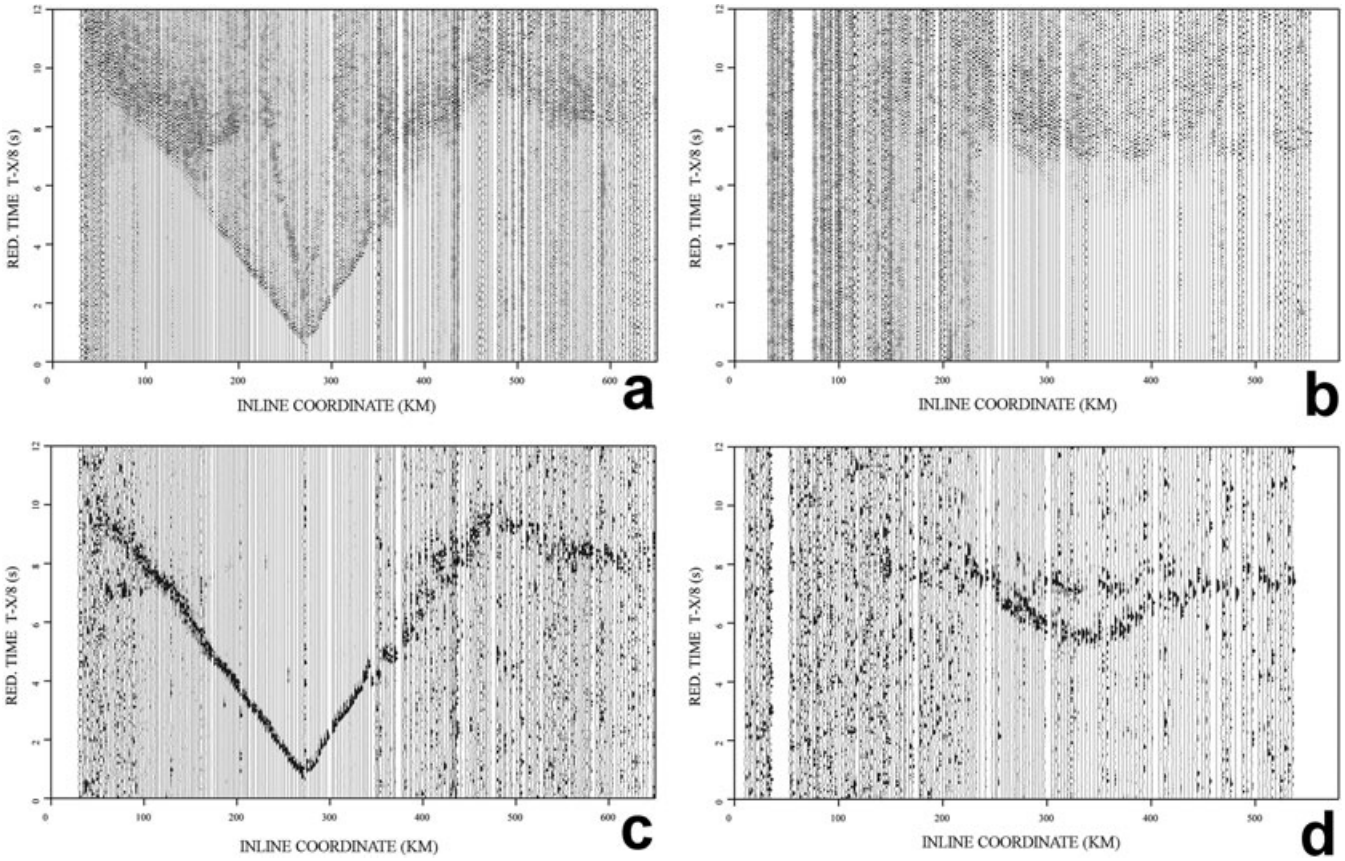

Figure 5. Original record sections (a, b) and resulting sections from application of STA/LTA signal detection (c, d), reduced with 8 km s^{-1}. Record sections a, c show an inline section recorded on a N-S oriented profile crossing the Eastern Alps. Record sections b, d show a crossline section recorded on a WNW-ESE oriented profile across the Eastern Alps the External Dinarides and the Pannonian Domain. STA/LTA-processed traces are used for stacking of *Pg* and *Pn* waves, but not for *PmP* waves.

decomposed according to

$$t(aoff) = td_{SRC} + \frac{aoff}{v_{Pn}} + td_{RCV} \tag{1}$$

with, t, travel time of a refracted wave (here: *Pn*); td_{SRC}, td_{RCV}, refractor (here: Moho) delay times at source and receiver locations; *aoff,* absolute offset; v_{Pn}, refractor velocity at the CMP-location.

2-D and 3-D refraction surveys lead to equation systems based on (1) which can be solved for laterally variable delay times and refractor velocities. In case of a 1-D velocity distribution $v_{Pg}(z)$ above and a constant velocity v_{Pn} below the refractor (Moho), the delay time *td* and the depth *D* of the refractor at an arbitrary location are related by:

$$td = \int_{z=0}^{z=D} \sqrt{\frac{1}{v_{Pg}(z)^2} - \frac{1}{v_{Pn}^2}} \cdot dz \tag{2}$$

In case of a dipping refractor or lateral variations of v_{Pg} the delay time depends on the azimuth of the ray. Such effects cannot be resolved by the delay time model and degrade the accuracy and resolution of the solution. However, these effects can be minimized by survey sinking of the data set to a new reference datum close to the refractor (Fig. 9b). This procedure provides a simulation of an experiment where shots and receivers are located on a datum near the refractor. Such techniques are very common in reflection seismic surveys with proper spatial sampling where the downward continuation of the wave field is based on application of the wave equation (Claerbout, 1985; Yilmaz, 2001). The spatial sampling of the seismic wave field by WAR/R experiments does not meet the requirements for downward continuation based on the wave equation. Therefore our method is based on ray tracing. Travel times at a new, deeper datum are calculated by taking the ray path from the original to the new source and receiver locations into account. The ray geometry (SRC-, RCV-, CMP-locations, *aoff*) is further modified (Fig. 9b). We choose the depth level Z = 33 km as the new (flat) reference datum and the crustal velocity model $v^s{}_{Pg}$ for ray tracing. A detailed description of the method based on ray tracing is given in Appendix D. The following procedures concerning *Pn* phases refer to traces after the survey sinking to the new datum.

The delay time model as given by eq. (1) does not take vertical velocity gradients of the refracting layer into account, although this is probably the case in the uppermost mantle. In order to increase the coherency of the *Pn* arrivals prior to stacking, we assume a constant vertical velocity gradient (k_{Pn}). Lateral variations of k_{Pn} cannot be resolved with the data set. The travel time difference Δt_{grad} caused by the gradient is approximated by:

$$\Delta t_{grad} = \frac{x}{v_{Pn}} - \frac{2}{k_{Pn}} \cdot \mathrm{a\,cosh}\left(\frac{\sqrt{4 \cdot v_{Pn}^2 + k_{Pn}^2 \cdot x^2}}{2 \cdot v_{Pn}}\right) \tag{3}$$

The first term in (3) is the travel time for a ray with the offset x in a zero gradient layer with the velocity v_{Pn}, and the second term is the

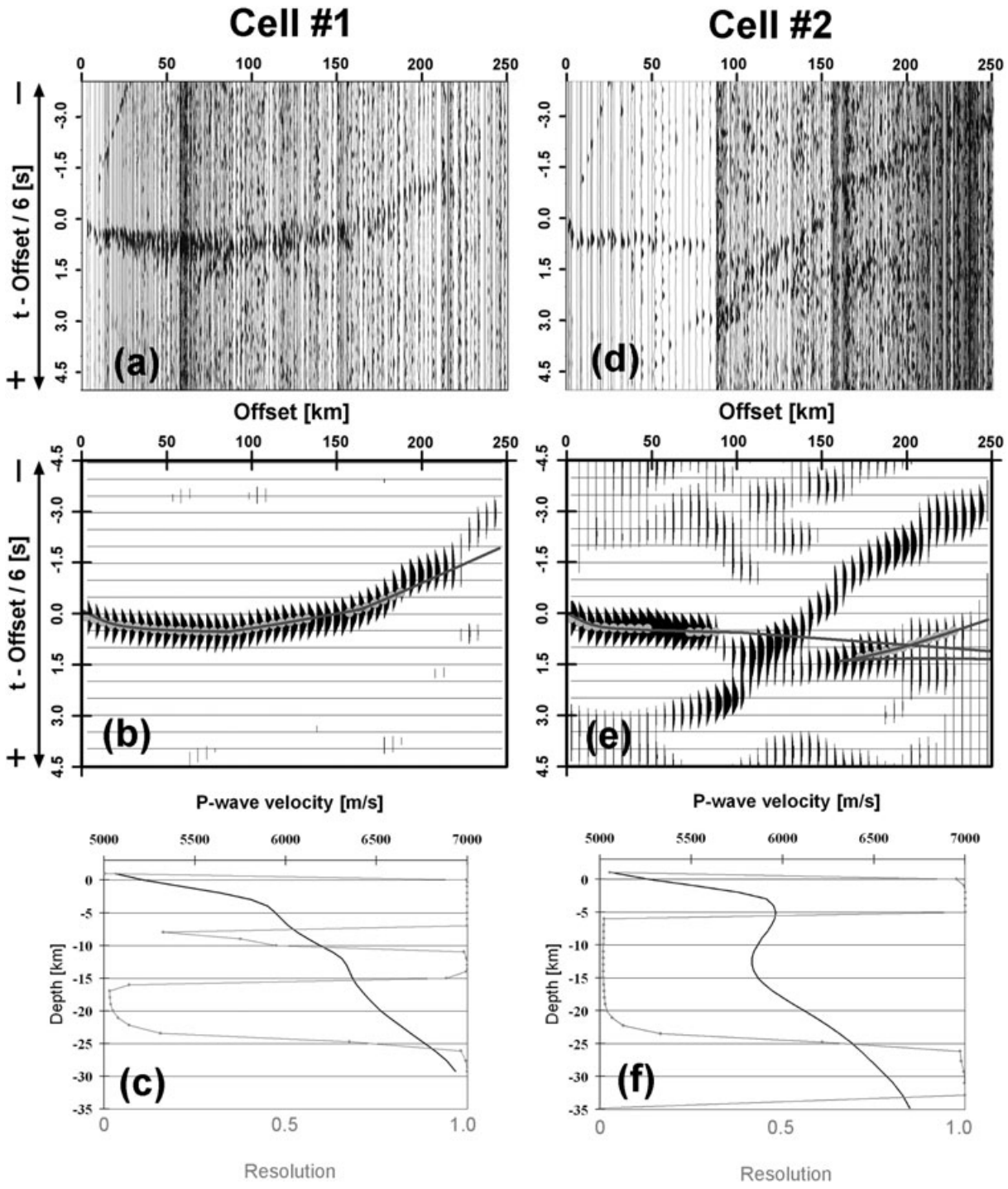

Figure 6. Steps towards a velocity-depth function for the crust illustrated for two selected cells (#1, #2). Upper row (a, d): CMP-gather for the cells after the application of static corrections (LMO-reduced with 6 km s^{-1}). Negative time is upward. Middle row (b, e): Low pass filtered and differentiated OFB-stacks for the cells (LMO-reduced with 6 km s^{-1}). Negative time is upward, and negative amplitudes are masked. Light grey circles: interpreted travel time picks. Dark grey line: Calculated travel time curve. Note the interpreted shadow zone in (e) in the offset range between 100 and 160 km, which results in a low velocity zone in the velocity model (f). Lower row (c, f): Resulting velocity models v(z) (black line) and the resolution elements (thin grey line). Note the almost zero resolution in depths corresponding to offset ranges where no picks were made.

travel time for a refracting layer (gradient k_{Pn}). The offset x (distance between the piercing points of the ray at the Moho boundary) is approximated by *aoff* at the new datum, and the influence of the velocity gradient on the ray path in the crust is neglected. All traces are shifted by Δt_{grad} assuming a velocity of $v_{Pn} = 8000$ m s^{-1} and a vertical velocity gradient of $k_{Pn} = 0.005$ s^{-1}.

Refractor delay times *td* and velocities v_{Pn} are specified for cells centred on grid points and are calculated based on eq. (1). Rearranging (1) leads to:

$$\frac{aoff}{v_{Pn}} = t(aoff) - (td_{SRC} + td_{RCV}) \tag{1a}$$

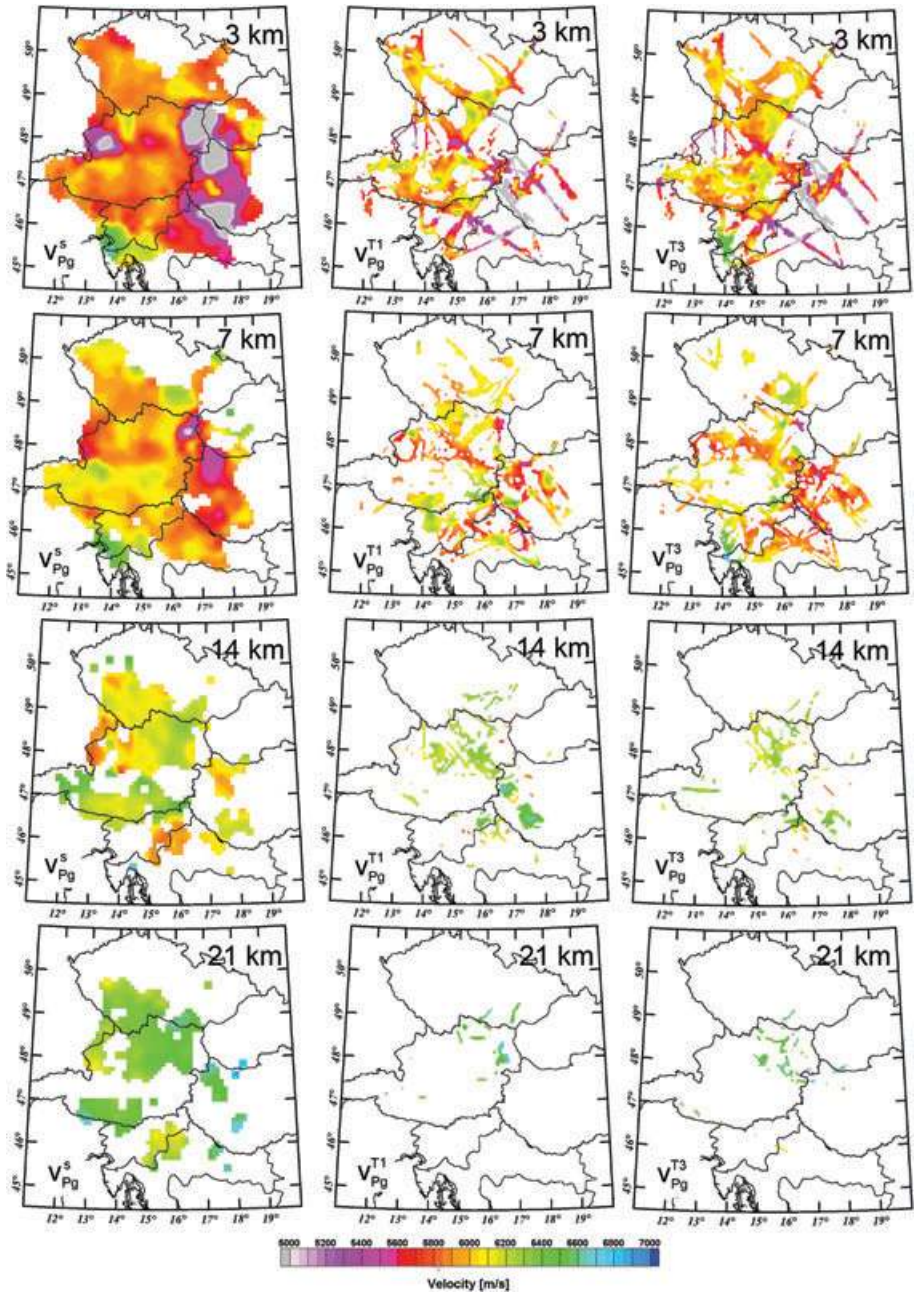

Figure 7. Depth slices at Z = 3, 7, 14, and 21 km through the velocity models $v^{s}{}_{Pg}$ (left column), $v^{T1}{}_{Pg}$ (middle column; only shown in areas with ray coverage), and $v^{T3}{}_{Pg}$ (right column; only shown in areas with ray coverage). $v^{T1}{}_{Pg}$ and $v^{T3}{}_{Pg}$ result from 3-D tomographic inversion (*cf*. Section 5).

(1a) implies that v_{Pn} of a cell corresponds to the slope of assigned *Pn* phases *t(aoff)* which are arranged along their absolute offset. In case of stacked data, v_{Pn} is the slope of the OFB-stack. If estimates of delay times are available prior to stacking, time corrections $(td_{SRC} + td_{RCV})$ are applied to the traces to improve the coherency of the phases. The half intercept time of the OFB-stack is a first approximation, td_0, of the delay time of the cell. More accurate delay times are derived from stacking SRC&RCV-sorted *Pn* phases. We have to rearrange eq. (1) to calculate the delay time from SRC&RCV-sorted *Pn* phases:

$$td = t(aoff) - (td_{RCV} + \frac{aoff}{v_{Pn}}) \tag{1b}$$

$$td = t(aoff) - \left(td_{SRC} + \frac{aoff}{v_{Pn}}\right) \tag{1c}$$

Prior to SRC&RCV-stacking we have to discriminate between cases where the source or the receiver of the trace is located within the cell. In case the source is located within the cell, the trace is time corrected for the delay time at the receiver location (eq. (1b)). In case the receiver is located within the cell, the trace is time corrected for the delay time at the source location (eq. (1c)). In both cases the trace is further time corrected for the ray path through the refractor as calculated from the *Pn* velocity at the CMP-location and the absolute offset.

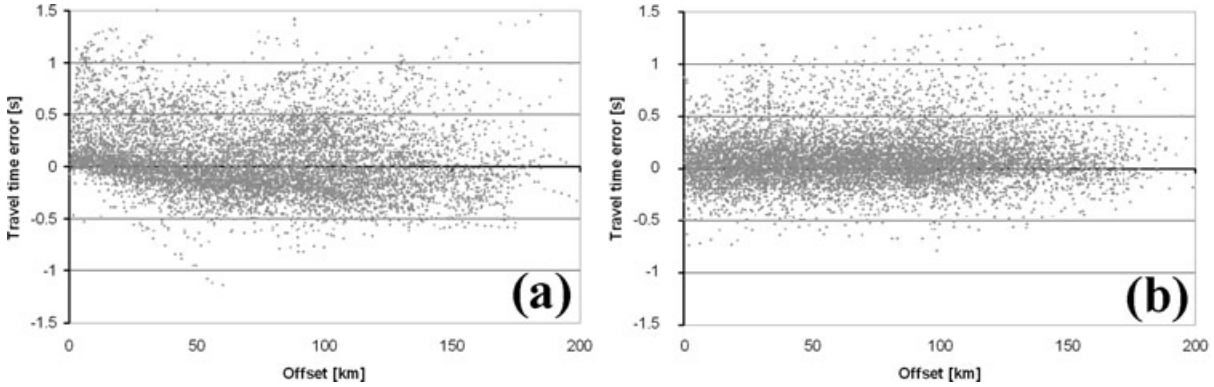

Figure 8. (a) Travel time residuals of *Pg* phases calculated with model v^s_{Pg} (b)Travel time residuals of *Pg* phases calculated with the final model of the crust, v_{Pg} (*cf*. Section 5).

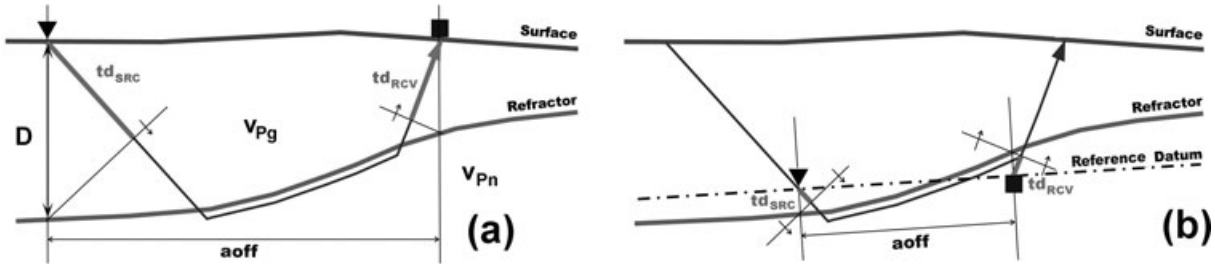

Figure 9. Illustration of the principles of delay time decomposition (a) and survey sinking (b) of a refracted ray to a new reference datum. Triangles: shots. Rectangles: receivers. v_{Pg} is the velocity above the refractor interface, and v_{Pn} is the velocity below the refractor interface. (a): The datum is the surface. td_{SRC}, td_{RCV}: Shot and receiver delay times. A off: Absolute offset. D is the depth of the refractor. (b): The new reference datum is close to the refractor. Shot and receiver locations have moved along the ray path to the reference datum. td_{SRC} and td_{RCV} are the new delay times at the reference datum, *aoff* is the new offset. In this case, td_{SRC} is positive (refractor below reference datum) and td_{RCV} is negative (refractor above reference datum).

The determination of velocities and delay times by (1a) to (1c) is an iterative procedure because of the mutual dependency of the parameters. In the following sections we describe the algorithm in more detail.

4.4.2 OFB-stack

The parameters chosen for the OFB-stacks of *Pn* phases are $l_G =$ 20 km (grid spacing), $l_C = 160$ km (cell size), $l_B = 5$ km (bin size), and LMO velocity $= 8\ \mathrm{km\,s^{-1}}$ (reduction velocity v_{red}). The cell size has been chosen so large in order to achieve a smooth and robust *Pn* velocity solution. The OFB-stacks are τ-p-transformed for a convenient and accurate extraction of slope (Δp) and intercept time (τ) from the stack. Fig. 10a shows an OFB-stack without time corrections ($td_{SRC} + td_{RCV}$) (eq. (1a)), and Fig. 10b shows its τ-p transform A first approximation of the delay time is $td_0 = \tau/2$. Since the data are reduced by $8\ \mathrm{km\,s^{-1}}$, the slowness improvement to the reduction velocity, Δp, is determined and the velocity v_{Pn} is calculated according to eq. (4):

$$\frac{1}{v_{Pn}} = \Delta p + \frac{1}{v_{red}} \tag{4}$$

OFB-stacks are created for all cells with sufficient data coverage and a robust *Pn* velocity solution v_{Pn} and the delay time estimate td_0 are derived.

4.4.3 SRC&RCV-stack

The parameters for SRC&RCV-stacks of *Pn* phases were selected as $l_G = 10$ km (grid spacing), $l_C = 40$ km (cell size), and LMO velocity $= 8\ \mathrm{km\,s^{-1}}$ (reduction velocity). Time corrections according to eqs. (1b) and (1c) are applied with v_{Pn} at the CMP location and td_0 at the source and receiver locations. Fig. 11 shows the SRC&RCV-gather of a cell and its stack. The determination of delay times by SRC&RCV-stacking starts also from the initial values td_0. New delay times *td*' are picked from the SRC&RCV-stacks (Fig. 11b) and improved delay times td_1 are calculated by eq. (5):

$$td_1 = td_0 + \frac{td' - td_0}{2} \tag{5}$$

The half difference to the previous solution is applied since the improvement accounts both for the cell location and the location at the complementary end of the ray. An iteration loop is started which uses the improved delay times td_1 for the time corrections (1b) and (1c). The sequence of the loop is: (1) calculating time corrections, (2) SRC&RCV-stacking, (3) picking delay times, and (4) applying eq. (5). The loop is stopped when the second term in eq. (5) approaches zero. We derive a stable delay time solution after 3 iterations. An updated velocity solution v_{Pn} is calculated (Section 4.4.2), and at this stage delay time corrections ($td_{SRC} + td_{RCV}$) are applied according to (1a) prior to OFB-stacking (Figs 10c and 10d). As a next step, the whole iterative procedure to determine improved delay times starts again with SRC&RCV-stacking. As no significant modifications could be yielded by further updating the *Pn* velocity, we regard these models as the final outcome from the stacking procedure and denote them as td^s and $v^s{}_{Pn}$. Two slices through the final 3-D volume of the SRC&RCV-stacks are shown in Fig. 12, and the models td^s and $v^s{}_{Pn}$ are shown in Fig. 13.

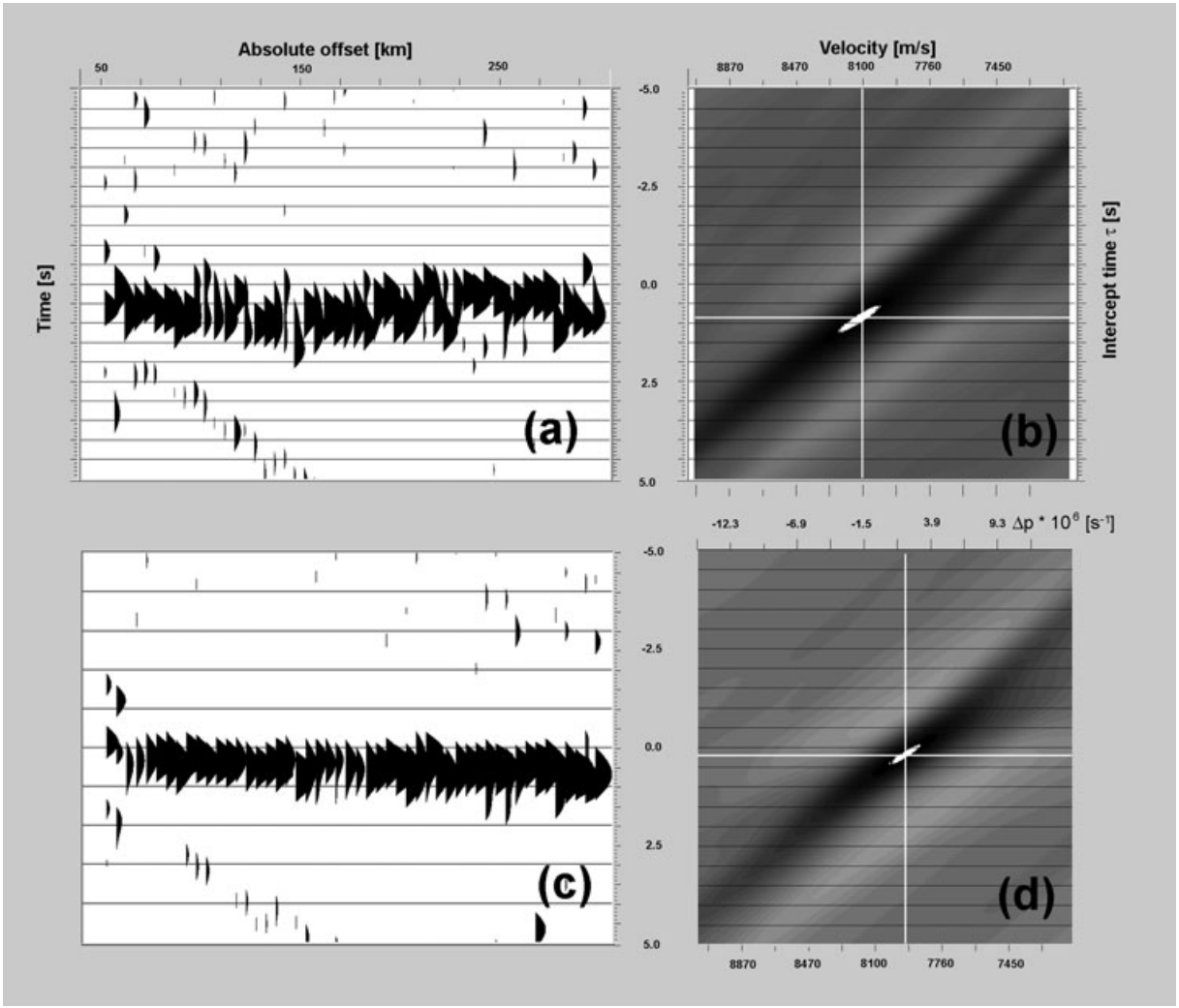

Figure 10. (a) Low pass filtered and differentiated OFB-stack of CMP-sorted *Pn* waves of a selected cell. Negative amplitudes are masked. (b) The τ-p transform of (a). The white ellipse corresponds to the maximum amplitude of the τ-p transform and its centre defines the picked intercept time τ and the slowness improvement Δp. The upper horizontal axis is the *Pn* velocity of the cell calculated according to eq. (4). (c) and (d) as (a) and (b), but delay times have been applied as time corrections prior to stacking.

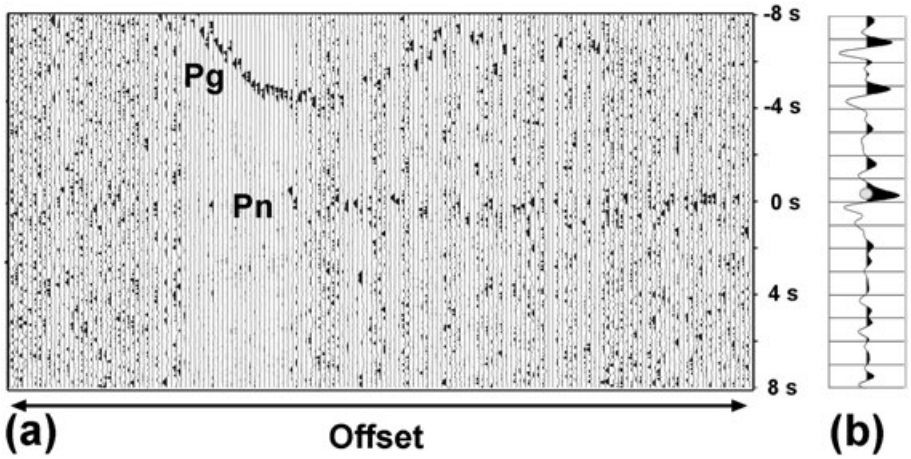

Figure 11. (a) SRC&RCV-gather for a selected cell of downward continued traces. The traces are time corrected for v_{Pn}, for an assumed upper mantle gradient, and for a linear moveout velocity of 8 km s^{-1}. Zero time is equal to the depth of the reference datum (Z = 33 km). The traces are equidistantly arranged along the horizontal axis according to their absolute offset. (b) Low pass filtered and differentiated SRC&RCV-stack of (a). Light grey circle: interpreted delay time pick td'.

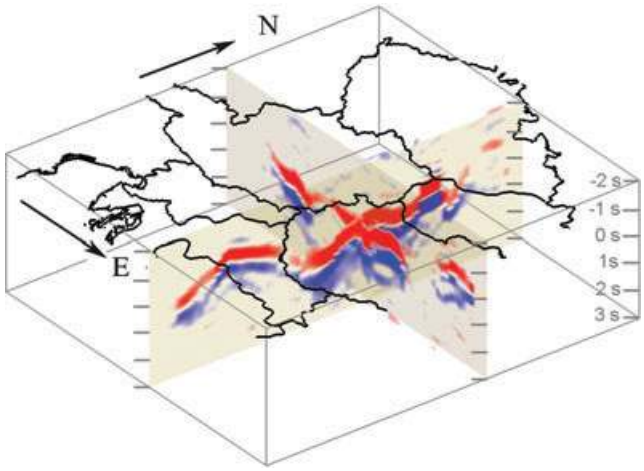

Figure 12. Two cross-sections through the 3-D volume of low pass filtered and differentiated SRC&RCV-stacks of *Pn* waves. The lateral extent of the surrounding box is 600 km E-W and 660 km N-S. Top view from SE. Zero time corresponds to the reference level Z = 33 km (survey sinking). Red colours indicate positive amplitudes and blue colours indicate negative amplitudes of the stacks.

4.4.4 Processing Flow

Since the stacking and inversion of *Pn* phases is not as straightforward as for *Pg* phases, we summarize the important steps which are applied to the data in this section:

(1) Survey sinking to the datum Z = 33 km

(2) Travel time correction for a vertical velocity gradient in the uppermost mantle and LMO-correction with $v_{red} = 8$ km s^{-1}.

(3) OFB-stacking yields a first velocity solution v_{Pn} and a rough initial estimate of the delay times, td_0.

(4) SRC&RCV-stacking starting with time corrections calculated from v_{Pn} and td_0.

(5) Picking delay times from the SRC&RCV-stacks, and updating the initial/previous delay time solution; Replacing the initial/previous delay time solution by the updated delay time solution *td* and go back to step (4) until convergence of *td* is achieved.

(6) OFB-stacking, using *td* as time corrections, yields a final velocity solution $v^s{}_{Pn}$.

(7) SRC&RCV-stacking starting with time corrections calculated from $v^s{}_{Pn}$ and *td*.

(8) Picking the final delay times td^s from the SRC&RCV-stacks.

4.4.5 Calibration with record travel times

The 2940 *Pn* picks (t_{obs}; Fig. 2b) are also downward continued to Z = 33 km and are used to check the accuracy of the delay time model and to calibrate the travel times picked from the stacked traces (Behm, 2006). Travel times t_{calc} are calculated according to eq (1) with delay times td^s at the source and receiver stations and the *Pn* velocity $v^s{}_{Pn}$ at the CMP-location, including the correction for the vertical velocity gradient of the upper mantle (4). The travel time residuals $dt = t_{obs} - t_{calc}$ are −0.34s on average, and the RMS error is 0.26 s (Fig. 14a). The negative average residual implies that the delay times derived from stacking on average are 0.17 s higher than the true travel times interpreted in the record sections. As pointed

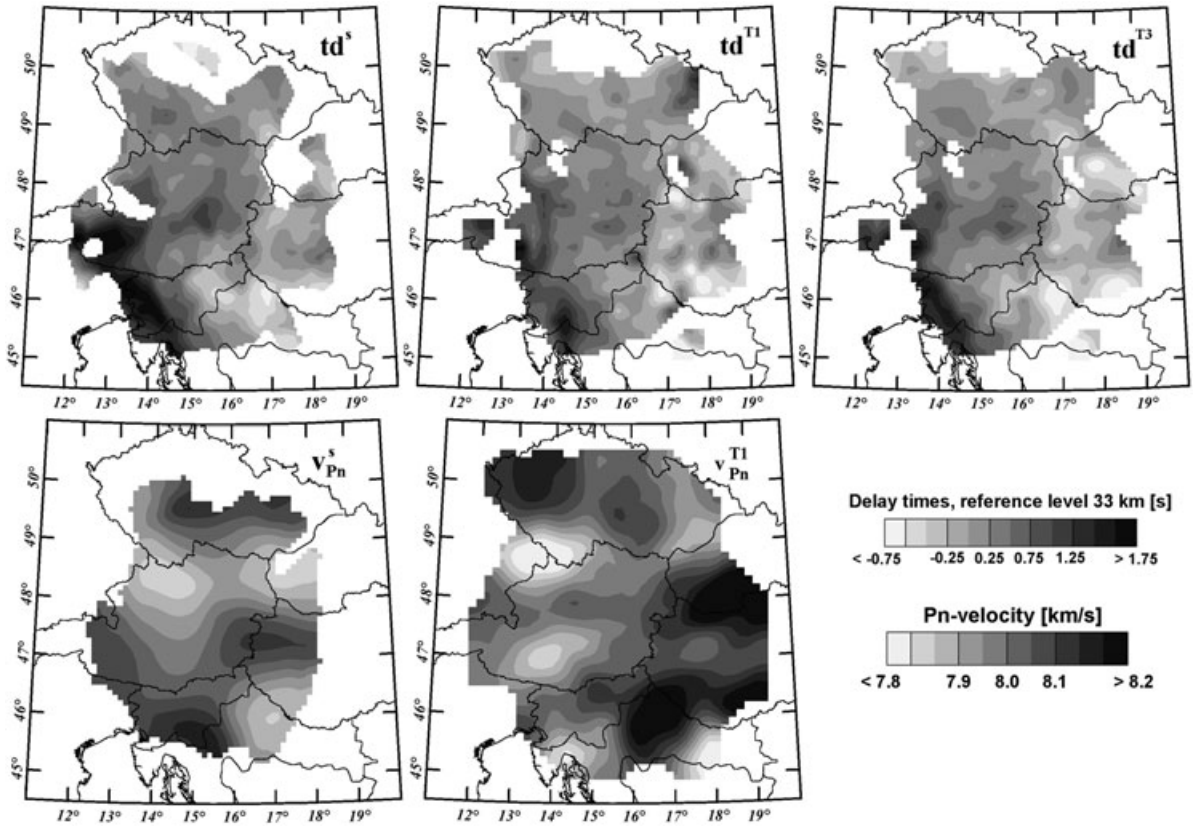

Figure 13. *Pn* delay times and *Pn* velocity models. Upper row: *Pn* delay time models td^s, td^{T1} (*cf*. Section 5) and td^{T3} (*cf*. Section 5) Lower row: *Pn* velocity model $v^s{}_{Pn}$ and $v^{T1}{}_{Pn}$ (*cf*. Section 5).

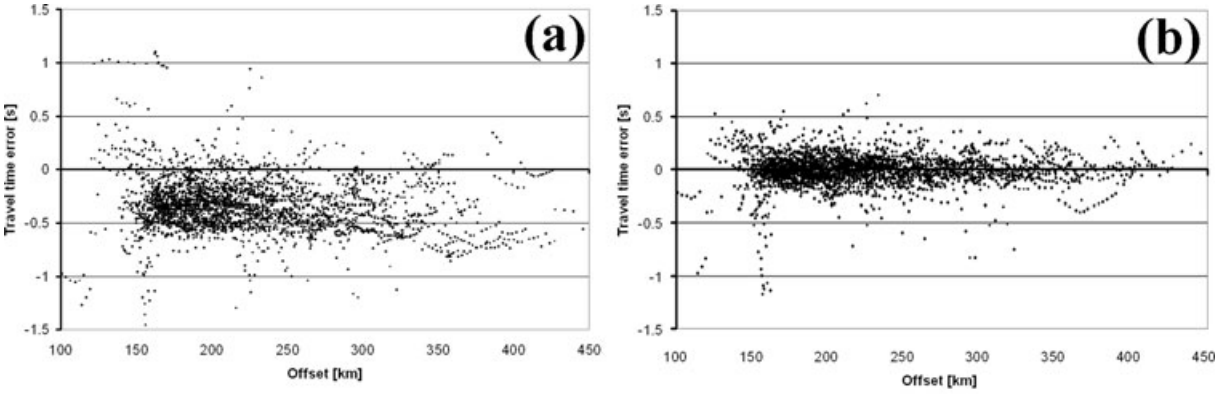

Figure 14. (a) Travel time residuals of *Pn* phases calculated with models td^s and v^s_{Pn}. (b) Travel time residuals of *Pn* phases calculated with the final delay time models td and v^s_{Pn} (*cf*. Section 5).

out in Section 4.4.2 there is some uncertainty in defining the arrival time of a stacked phase. Therefore, we subtract 0.17 s from the delay times td^s in order to calibrate them to record travel times. Fig. 14a shows also an offset dependency corresponding to a systematic underestimation (45 m s^{-1}) of the velocities by model v^s_{Pn}. This little deviation is not considered further, as it could also be attributed to an incorrectly assumed velocity gradient of the uppermost mantle.

4.4 Stacking of *PmP*-phases

Our processing of the wide-angle reflection data is based on the principles of standard processing of CMP-sorted reflection seismic data (e.g. Yilmaz, 2001; ECORS-CROP Deep Seismic Sounding Group *et al.* 1989) and transformation of trace amplitudes to complex amplitudes (Valasek *et al.* 1991). We did not apply the STA/LTA algorithm since we are interested in the reflection band waveform not just in the onset of reflected energy.

Trace editing and offset limitation to 220 km reduced the number of traces to 20417. The parameters of CMP-sorting are $l_G = 10$ km (grid spacing) and $l_C = 40$ km (cell size). The effect of near surface velocity variations is removed by survey sinking to the datum Z = 10 km, which is superior to simple static corrections we use the crustal velocity model v^s_{Pg} and optimize the ray parameter for *PmP* reflections from a Moho depth of 33 km (Appendix C). For each cell, constant velocity stacks (velocity gathers) are created to determine the optimum V_{nmo} for *PmP* below Z = 10 km by visual inspection. V_{nmo} below 10 km depth varies between 6200 m s^{-1} and 6750 m s^{-1} with an average value of 6450 $\pm$ 90 m s^{-1}. The data is stacked after normal moveout correction with V_{nmo}. Fig. 15 shows two cross sections through the 3-D volume of the CMP-stacks, from which *PmP* two way normal incidence travel times $T0^s$ (Fig. 16) were picked. In some areas (hatched area in Fig. 16) reflections from the lower crust mask the stacked *PmP* waves. Although these reflections give valuable information on the structure of the crust, they have not been considered further in this paper.

4.5 Summary of the stacking methods

The different modelling strategies for the crust and uppermost mantle, the accompanying sorting, binning, and stacking routines as well as the necessary time corrections are summarized in Table 1.

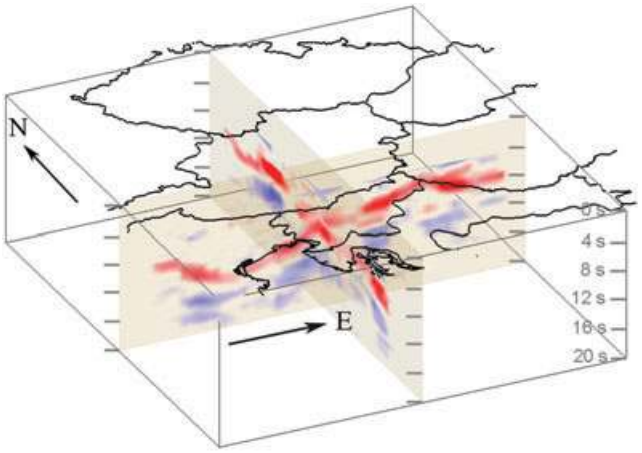

Figure 15. Two cross-sections through the 3-D volume of low pass filtered and differentiated CMP-stacks of wide-angle reflections. The lateral extent of the surrounding box is 600 km E-W and 660 km N-S. Top view from SSW. Zero time corresponds to the reference datum Z = 10 km. Red colours indicate positive amplitudes and blue colours indicate negative amplitudes.

5 IMPLEMENTATION OF RECORD TRAVEL TIMES

The stacking methods presented in Section 4 use a large data subset (34301 traces for *Pg*, 20727 traces for *Pn*, 20714 traces for *PmP*) and yield robust models with large coverage. The number of record travel times in the original sections is smaller (9531 *Pg* and 2940 *Pn*, Fig. 2) and we expect a relatively sparse coverage of a seismic 3-D model derived from record travel times only. On the other hand, these record travel times need no calibration and supply detailed information such that inversion of these times should provide high resolution. In this section we demonstrate how an optimized 3-D model may be created from the combination of models derived from stacking and record travel times.

5.1 3-D first arrival tomography of *Pg* record travel times

We calculate models based on 3-D first arrival tomographic inversion of the 9531 *Pg*- record travel times using the program by Hole (1992). The velocity cells have side lengths of 1 km. The iteration schedule is split into several parts, with different settings for the

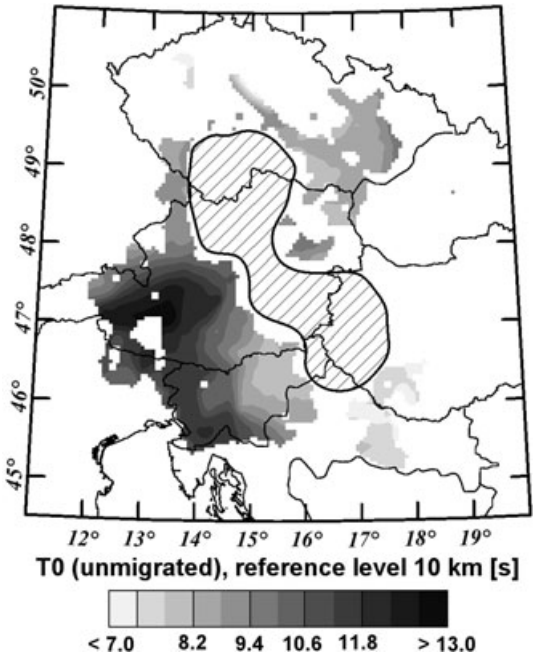

Figure 16. Two way travel time model T0^s (reference level Z = 10 km), derived from *PmP* stacks. The lack of information in the eastern and northern part (hatched area) is due to strong reflections from the lower crust which hindered reliable picking.

parameters at each iteration step. This is a commonly used routine, by which the upper layers are first constrained by restricting the considered offset. Furthermore, the size of smoothing filters is stepwise decreased during the course of the iterations for each selected offset interval.

We use two initial models for the tomographic inversion. The first initial model is a 1-D velocity-depth function given by eq. (6) and the resulting 3-D tomographic velocity model is called $v^{T1}{}_{Pg}$.

$$v^{1D}_{Pg}(z) = A \cdot (B + z)^{1/6} \quad (6)$$

The variable z is depth in meters. A velocity-depth function of the form given by eq. (6) is often used in applied geophysics (Faust, 1951). $A = 1125$ and $B = 14700$ were chosen to fit the average of $v^s{}_{Pg}$. The RMS error of the travel time residuals calculated with model $v^{1D}{}_{Pg}$ is 0.656 s. Below 15 km depth, $v^{1D}{}_{Pg}$ is close to the global average velocity for orogens (Christensen & Mooney, 1995). After 18 iterations the RMS error of $v^{T1}{}_{Pg}$ is 0.13 s. The dimension of the last smoothing filter was 16 km × 16 km × 2 km.

The second initial model was the 3-D model $v^s{}_{Pg}$ derived by the stacking methods. The tomographic inversion resulted in the model $v^{T3}{}_{Pg}$ after 6 iterations. The final RMS error is 0.12 s and the dimension of the last smoothing filter was 8 km × 8 km × 2 km.

Depth slices through both 3-D tomographic models $v^{T1}{}_{Pg}$ and $v^{T3}{}_{Pg}$ are shown in Fig. 7 together with the corresponding depth slices through $v^s{}_{Pg}$. Model $v^{T3}{}_{Pg}$ has a slightly better coverage than $v^{T1}{}_{Pg}$. Tests with synthetic models show further that velocity anomalies are better reproduced when a realistic 3-D initial model is used instead of a best-fitting 1-D initial model (Behm 2006). In particular high velocity regions in the uppermost crust cannot be restored using an average 1-D initial model. We attribute this to the dependency of the ray geometry on the velocity model. Therefore we conclude that the choice of an appropriate laterally variable initial model is important for successful application of 3-D tomographic inversion. Since the RMS error of $v^s{}_{Pg}$ is only half the RMS error of $v^{1D}{}_{Pg}$, we consider $v^s{}_{Pg}$ as a more realistic initial model than $v^{1D}{}_{Pg}$. In other words, the model resulting from the stacking technique is probably closer to the global minimum than the best-fitting 1-D initial model. Subsequently, we consider $v^{T3}{}_{Pg}$ as a more reliable model and discard $v^{T1}{}_{Pg}$.

5.2 Combination of the velocity models derived from stacking and 3-D tomography

The models $v^{T3}{}_{Pg}$ and $v^s{}_{Pg}$ exhibit the same large-scale structures (Fig. 7). The standard deviation of the velocity difference $v^{T3}{}_{Pg} - v^s{}_{Pg}$ is 320 m s^{-1} at Z = 0 and 150 m s^{-1} at Z = 5 km. Between 10 and 20 km depth, the standard deviation of the difference is about

Table 1. Summary of the applied stacking techniques

Aim	Used phase	Sorting, Binning, Stacking, Picking	Time corrections prior to stacking
Local velocity-depth functions of the crust	*Pg*	Sorting to CMP-gathers	LMO reduction with 6 km s^{-1}
		Stacking in offset bins Picking smooth 1-D travel time curves	Static corrections accounting for near surface layers
Laterally varying uppermost mantle velocity	*Pn*	Sorting to CMP-gathers	Survey sinking to Z = 33 km
		Stacking in offset bins Picking *Pn* velocities from τ-p-transforms	Velocity gradient in the uppermost mantle LMO reduction with 8 km s^{-1} Time corrections accounting for the travel time through the crust (delay times)
Moho topography expressed as delay times	*Pn*	Sorting to SRC&RCV- gathers	Survey sinking to Z = 33 km
		Stacking in SRC&RCV cells Picking delay times	Velocity gradient in the uppermost mantle LMO reduction with 8 km s^{-1} Time corrections accounting for the travel time through the uppermost mantle (*Pn* velocity) and for the delay time outside the cell
Moho topography expressed as two way travel times	*PmP*	Sorting to CMP-gathers	Survey sinking to Z = 10 km
		Stacking in CMP cells Picking two way travel times	NMO correction

100 m s^{-1}. For the uppermost crust, a detailed analysis shows a correlation of the velocity difference with the variation of the sedimentary cover such that $v^{s}{}_{Pg}$ provides higher velocities in sedimentary basins than $v^{T3}{}_{Pg}$. The mean velocity difference is +40 m s^{-1} below 3 km depth, which implies that, on average, model $v^{s}{}_{Pg}$ provides lower velocities (Behm, 2006).

Model $v^{s}{}_{Pg}$ covers a larger area and is based on deeper penetration than the tomographic model but has a small systematic velocity shift and lower resolution, as it is expressed by a larger RMS error. Travel time residual analysis and checkerboard tests for model $v^{T3}{}_{Pg}$ (Behm, 2006) show that, in particular in the uppermost crust, $v^{T3}{}_{Pg}$ is more accurate and has better resolution than $v^{s}{}_{Pg}$. Low velocities of sediments (1500–4000 m s^{-1}) are overestimated by model $v^{s}{}_{Pg}$ (300 – 500 m s^{-1} difference on average). However, this overestimation is not compensated by underestimation of velocities in deeper layers. This is deduced from the fact that record sections with shots inside a basin always show a large systematic shift of the travel time errors. It further suggests that inversion of stacked data is a robust method.

We conclude that the tomographic model $v^{T3}{}_{Pg}$ is superior to $v^{s}{}_{Pg}$ for the interpretation of local features in the upper crust, while $v^{s}{}_{Pg}$ is preferable for regional interpretations. However, by combining these two models we derive an integrated and final 3-D velocity model of the crust, v_{Pg}, which takes the advantage of both approaches.

A simple combination or calculation of the average of the two models would result in artificial velocity discontinuities due to the differences in velocities and the different coverage. Therefore, a more elaborate approach is applied which also takes the lateral resolution of the data into consideration (Behm, 2006).

Model $v^{T3}{}_{Pg}$ comprises changes to $v^{s}{}_{Pg}$. Due to its nature, the 3-D tomographic model has smaller travel time residuals and contains high frequency improvements to $v^{s}{}_{Pg}$. Based on the method by Zelt (1998), $v^{T3}{}_{Pg}$ is quantitatively examined for its lateral resolution. For each velocity $v^{T3}{}_{Pg}(x,y,z)$ an estimate of the lateral resolution, $R(x,y,z,)$, is derived. Possible artefacts in $v^{T3}{}_{Pg}$ are removed by low pass filtering $v^{T3}{}_{Pg}(x,y,z)$ with filter sizes adapted to $R(x,y,z)$. In areas with coverage in both models the difference between the filtered model $v^{T3}{}_{Pg}$ and model $v^{s}{}_{Pg}$ is calculated. At each depth, this difference is interpolated to full lateral coverage and added to $v^{s}{}_{Pg}$. This procedure corresponds to a calibration of $v^{s}{}_{Pg}$ by record travel times. The final model v_{Pg} (Fig. 17) has the same grid spacing and coverage as $v^{s}{}_{Pg}$, resolvable high frequency improvements are introduced, and artificial velocity discontinuities due to merging are avoided. The RMS error of v_{Pg} (Fig. 8b) is 0.26 s and the mean error is 0.095 s. The positive mean error with no offset dependency indicates that the uppermost layers are slightly too 'fast' in this model. Detailed error analyses (Behm, 2006) show that the large RMS error is mainly a result of the lateral grid size, which does not allow for full description of near-surface velocity variations.

5.3 *Pn* delay time tomography from record travel times

The delay time models of the Moho are improved by using 2940 *Pn* picks from record traces, downward continued to Z = 33 km (Fig. 2b). Instead of evaluating the velocity at the CMP location (eq. (1)), a tomographic approach for the ray paths along the refractor is used. The principles of this delay time decomposition are described by e.g. Kirchheimer (1988), Iwasaki (2002), Song *et al.* (2004). Both delay times and velocities are specified at grid points and reinterpolated to the shot and receiver (td) and ray path positions (v), respectively. The interpolation function is a Gaussian function with the distance as parameter. The Gaussian function is chosen for its smooth behaviour and for prevention of overshooting. It is widely used in Prediction Theory (Kriging) and has also been applied to seismology (e.g. Toomey, 1994).

Starting from an initial model, travel time residuals are used to solve for improvements of the model parameters (delay times and velocities on grid points). Truncated singular value decomposition (TSVD) is used for the inversion, such that resolution and covariance elements also are calculated. The model may be smoothed with a Gaussian function. A damping factor determines the relative importance of delay times and velocities, where either velocities or delay times can be held fixed. Starting with an arbitrary initial model, a sequence of iterations with different parameter specifications is applied.

A delay time model td^{T1} and $v^{T1}{}_{Pn}$ (Fig. 13) is calculated from an initial constant delay time (0.147 s) and initial constant velocity (8000 m s^{-1}), based on the experience from model td^{s}. The grid intervals are 20 km for td and 30 km for v_{Pn}. The RMS error decreases from 0.57 s (initial model) to 0.10 s during the iteration. There is an overall similarity between these models and those obtained from stacked data (Fig. 13). However, at the Alpine root td^{T1} provides smaller delay times than td^{s}. The velocity solutions $v^{s}{}_{Pn}$ and $v^{T1}{}_{Pn}$ differ in the southern part of the investigation area.

Resolution tests (Behm, 2006), including synthetic models and variation of grid sizes, show strong coupling between delay times and velocities. There is an irresolvable ambiguity between large delay times and low velocities at the Alpine root. Overall, the velocities are not as well constrained as the delay times. The robustness of the velocity model $v^{s}{}_{Pn}$ in comparison to $v^{T1}{}_{Pn}$ may be also partly attributed to the use of OFB-gathers derived from CMP-sorted traces instead of application of a tomographic approach along the ray path. Similar to the crust, we consider td^{s} and $v^{s}{}_{Pn}$ as more realistic initial models than any 1-D initial model. Therefore, we use the models td^{s} and $v^{s}{}_{Pn}$ as initial models and keep the velocity fixed during another inversion, such that $v^{s}{}_{Pn}$ is regarded as the final *Pn* velocity solution v_{Pn} to derive model td^{T3} (Fig. 13) with an RMS error of 0.11 s.

5.4 Combination of delay times derived from stacking and record travel times

The model td^{T3} contains high frequency improvements $\Delta td(x,y)$ to the initial model td^{s} Similar to the crustal model, an integrated model td is calculated as a combination of td^{s} and td^{T3} taking the resolution of the travel time data into account (Behm 2006). The resolution of td^{T3} is expressed by the laterally varying resolution elements $r(x,y)$ of the improvements $\Delta td(x,y)$. In order to calculate an integrated model td, we damp the improvements Δtd according to the resolution elements r before adding Δtd to td^{s}. The damping factor $f(x,y)$ ranges between 0 and 1 is calculated from an empirical function (Fig. 18). The final delay time model td is calculated at each grid point according to eq. (7):

$$td = td^{s} + \Delta td \cdot f \tag{7}$$

Model td reproduces the picked *Pn* travel times within an RMS error of 0.151 s without offset dependency (Fig. 14b).

5.5 Combination of delay times and normal incidence times

The final model of depth to the Moho is derived by merging the delay times td with the two way normal incidence travel times $T0^{s}$. The delay times refer to the datum Z = 33 km, the two way normal

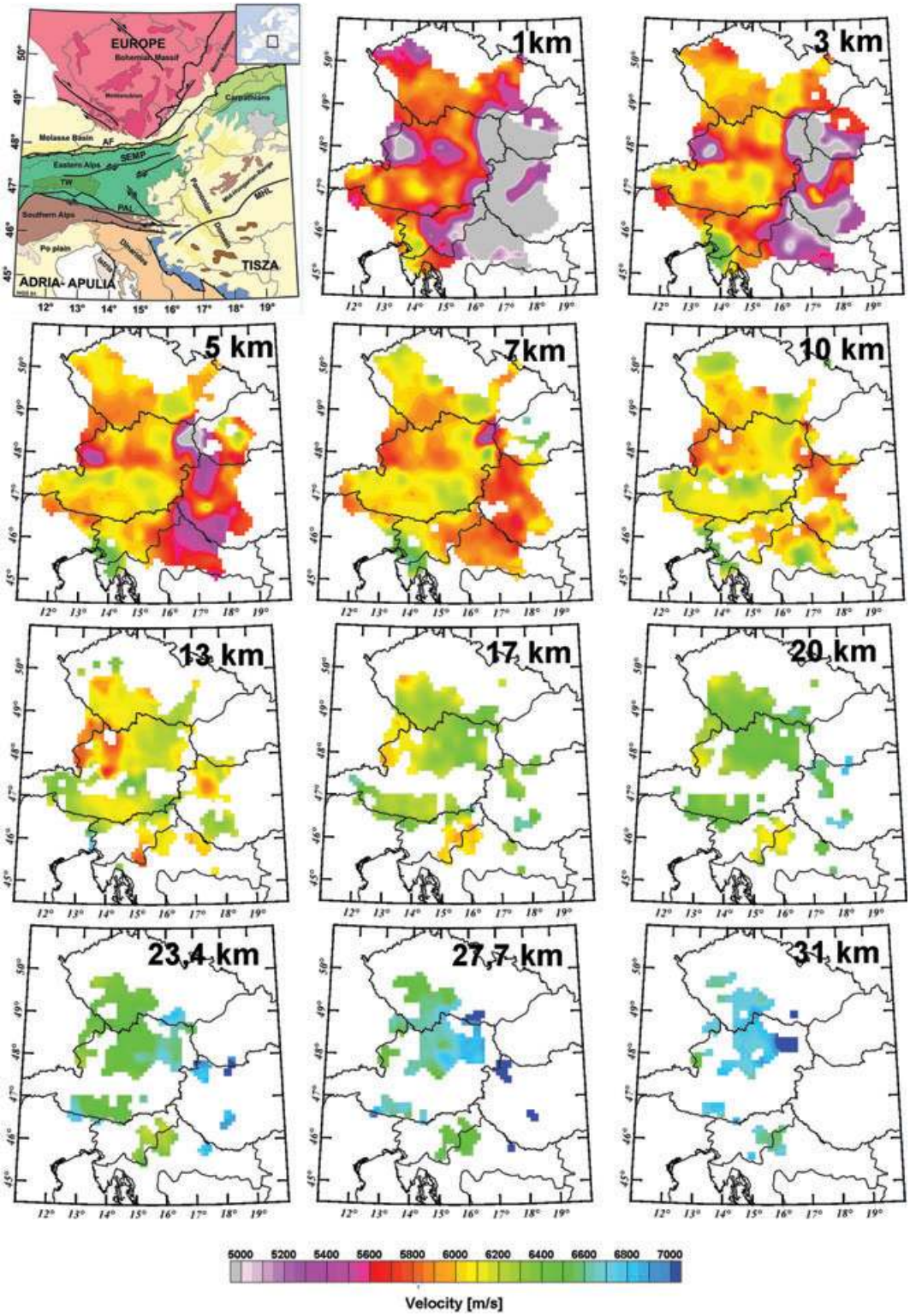

Figure 17. Depth slices through the final velocity model of the crust, v_{Pg}.

incidence travel times to Z = 10 km. We calculate *td* for Z = 10 km (Fig. 19) by eq. (8) at each grid point *(x,y)* and with the same velocity model as used for survey sinking:

$$td_{Z=10km} = td_{Z=33km} + \int_{z=10km}^{z=33km} \sqrt{\frac{1}{v_{Pg}^{s}(z)^2} - \frac{1}{v_{Pn}^{s\,2}}} \cdot dz \qquad (8)$$

We transform *td* to two way normal incidence travel times $T0^d$ at the datum Z = 10 km. This transformation, based on eq. (9), can be performed since delay times and normal incidence times are different measures of the Moho depth.

$$T0^d = \frac{\bar{s}}{\bar{q}} \cdot 2 \cdot td \qquad (9)$$

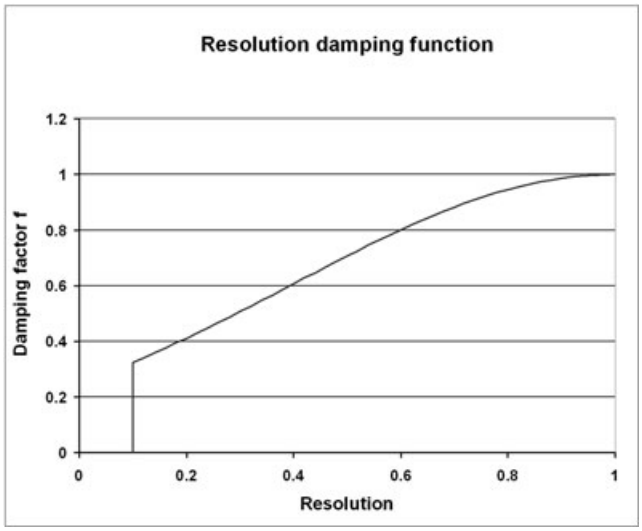

Figure 18. Resolution damping function for the combination of the delay times obtained from stacking and travel time inversion. The damping factor f (ordinate) ranges between 0 and 1 and increases with the resolution (abscissa).

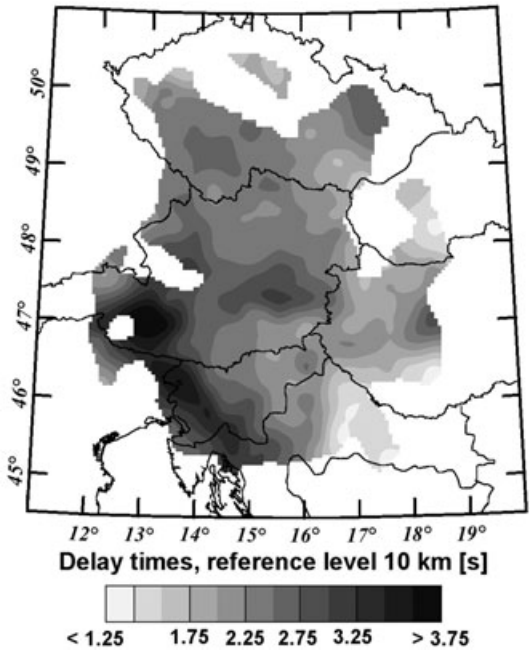

Figure 19. Final delay time model td (reference level Z = 10 km).

$\bar{s}$ is the mean slowness between the Moho and Z = 10 km, and $\bar{q}$ is the mean vertical slowness-component for a ray critically refracted from the Moho. The two quantities are calculated at each grid point by eqs. (9a) and (9b).

$$\bar{s} = \frac{\int_{z=10km}^{z=Z_M} \frac{1}{v_{Pg}(z)} \cdot dz}{Z_M - 10km} \tag{9a}$$

$$\bar{q} = \frac{\int_{z=10km}^{z=Z_M} \frac{1}{\sqrt{\frac{1}{v_{Pg}(z)^2} - \frac{1}{v_{Pn}^2}}} \cdot dz}{Z_M - 10km} \tag{9b}$$

Eqs (9), (9a), and (9b) are 1-D approximations. The Moho depth approximation Z_M is based on eq. (2) and the delay time model *td*. The error introduced by the transformation is estimated by differentiation of (9) assuming average values for *td* (2.3 s), v_{Pg} (6420 m s^{-1}) and v_{Pn} (7990 m s^{-1}). For uncertainties of ±0.1 s (td), ±100 m s^{-1} (v_{Pg}, v_{Pn}) the uncertainty of $T0^d$ is ±0.44 s, which corresponds to an error of ±1.4 km in the Moho depth.

The two way normal incidence travel times $T0^s$ are picked from stacks and should be calibrated by record travel times. As pointed out in Section 3, *PmP* waves can be identified in many record sections, but their exact arrival times are generally difficult to pick because they merge with other phases. We therefore calibrate $T0^s$ by $T0^d$, which is indirectly adjusted to the *Pn* record travel times. The average difference $T0^s - T0^d$ amounts to +0.2 s on average and is subtracted from $T0^s$. Finally $T0^d$ and the calibrated $T0^s$ are combined to the final, unmigrated two way normal incidence representation *T0* by taking the average in overlapping areas.

6 MAP OF DEPTHS TO THE MOHO

6.1 Structural interpretation

The 3-D volumes of the SRC&RCV-sorted *Pn* stacks and CMP-sorted *PmP* stacks provide insight into the structure of the Moho. Several cross sections indicate that the Moho in the investigation area is fragmented into three parts (Fig. 20). In the time domain, two lateral discontinuities or vertical offsets are clearly identified throughout the whole investigated area. They correlate with the strike directions of the Alps and the Dinarides. The three characteristic parts are: (1) 'EU' (associated with the European plate), (2) 'AD' (Adriatic-Apulian plates) and (3) 'PAN' (south-eastern part of the investigation area, associated with the Pannonian domain). Another lateral discontinuity in the stacks correlates with the Mid-Hungarian Line. Since the data coverage is sparse in this region, and the study focuses on the Eastern Alps, we do not consider this discontinuity further.

6.2 Depth migration

The two way travel times *T0* are shifted from 10 km depth to the reference datum Z = 0 km where they are time-migrated by the use of basic ray tracing, taking the fragmentation into consideration. The migration velocity at each grid point is approximated by the average velocity of the extrapolated model v_{Pg} between Z = 0 km and the Moho depth approximation Z_M. This results in the time-migrated two way travel time field $T0_{mig}$ (Fig. 21a). Depth conversion of $T0_{mig}$ with the extrapolated velocity model v_{Pg} leads to the Moho depth map (Fig. 21b). Gaps in the Moho surfaces originate from either the fragmentation into EU, AD, and PAN, or from lack of data.

6.3 Check by record travel times

The Moho depth model is checked after extrapolation to full coverage by 3-D ray tracing with the program ANRAY (Psencik, 1998). A total of 1710 rays can be traced out of the 2940 picked *Pn* arrivals (Fig. 2b). The relatively low hit rate is possibly a result of the Moho structure, which may be too complex for the ray-tracing algorithm to incorporate all observed arrivals. The average travel time residual

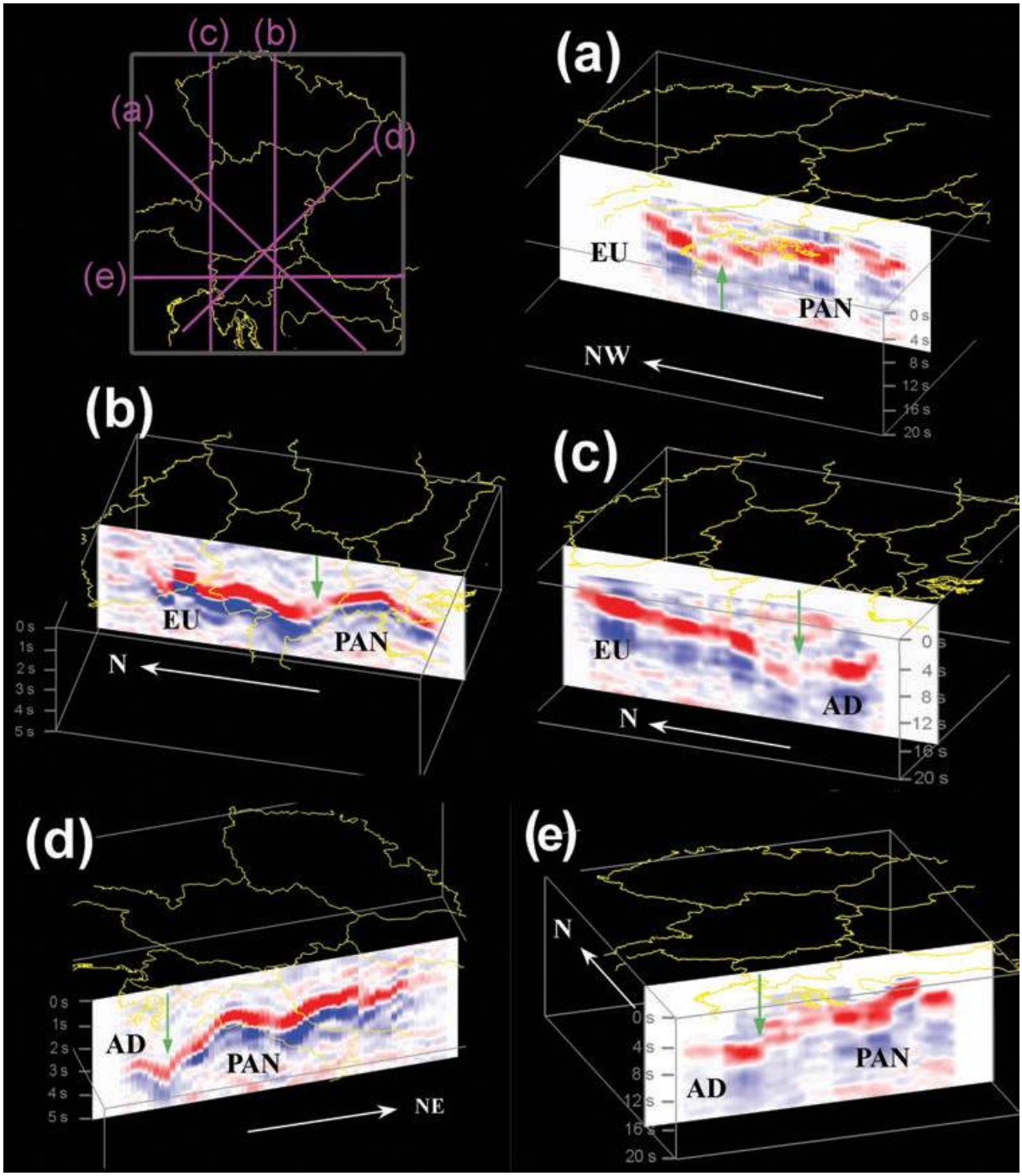

Figure 20. Five example cross-sections through the 3-D volume of SRC&RCV-stacks of *Pn* waves and CMP-stacks of *PmP* waves. The location of the cross-sections is shown in the upper left corner of the figure. All stacks are low pass filtered and differentiated. The reference level is Z = 10 km. The surrounding boxes have the same lateral extent as in Figs 12 and 15, respectively. The vertical length corresponds to 5 s (*Pn* stacks, (b), (d)) and 20 s (*PmP* stacks, (a), (c), (e)). Zero time, corresponding to the reference level Z = 10 km, is at the upper boundary of the boxes. The boundaries between the interpreted Moho parts (EU, AD, PAN) are indicated by green arrows. Although other boundaries are also visible, only those with pronounced lateral coherency are interpreted as lateral Moho boundaries.

is −0.14 s, and the RMS error is 0.36 s. A more detailed analysis of the travel time residuals has been performed by Behm (2006) who estimates the expected error of the Moho depths from the travel time residuals and further takes the inaccuracy of the *Pn* velocity model into account. On average, the Moho depth is overestimated by 0.8 km and its standard deviation amounts to ±1.3 km.

7 DISCUSSION

7.1 Stacking and inversion

Although regional aspects may have influence, we find that the basic conclusions in the following are in general valid for application of

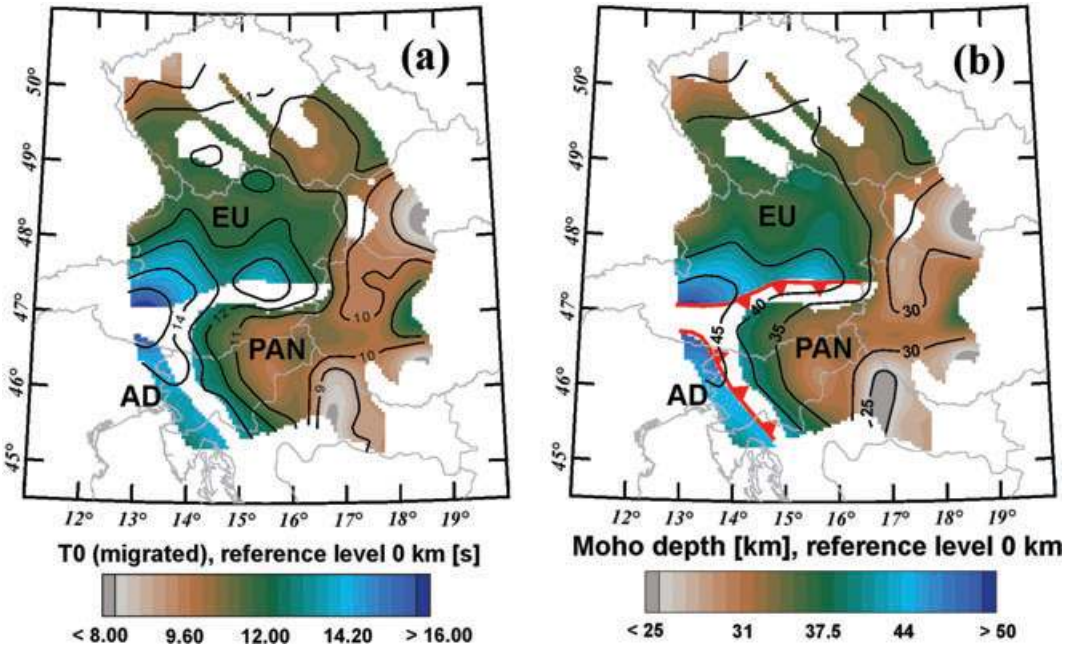

Figure 21. The Moho surface in time and depth. Gaps in the surfaces originate from either the fragmentation or from lack of data. The abbreviations EU (European plate), AD (Adriatic-Apulian plate) and PAN (Pannonian fragment) refer to the three interpreted Moho parts. (a) Migrated two way travel time model $T0_{mig}$ (reference level Z = 0 km). (b) Moho depth map (reference level Z = 0 km). Red signature indicates where underthrusting is interpreted.

stacking and inversion routines to 3-D WAR/R data. The stacking technique provides a basis for the generation of stable and robust models, which are close to the global minimum. To define these terms, we follow Tarantola (1987): 'Robustness' is insensitivity to outliers in the data, while 'stability' is insensitivity to small random errors in the data. Both are natural properties of stacking. Outliers may occur due to gross errors in static corrections or timing errors and will add to the noise level. Small random errors can be the result of inaccurate static corrections and will lead to a smeared stack. For stacking CMP-sorted traces over all azimuths, only a significant deviation from the 1-D assumption may result in a systematic shift of the stack.

Picking stacked phases is difficult in offset ranges around the crossover offset, because stacking and filtering the almost coincident *Pg*, *Pn* and *PmP* phases can result in a single long wavelet. More important, small systematic shifts in *Pg* and *Pn* velocities, *Pn* delay times and *PmP* two way travel times are inherent in stacked data since signal detection, stacking and low pass filtering is applied. The wavelet information is lost due to the transformation of trace amplitudes to envelopes. Therefore we define the maximum increase of amplitude of the stacked trace as the arrival time. Compared to single-fold data, the velocity models $v^s{}_{Pg}$ and $v^s{}_{Pn}$ are overall too slow ($\sim$0.05 km s^{-1}), whereas the *Pn* delay times td^s and the picked two way travel times $T0^s$ are on average too high (0.17 s and 0.2 s). This shows that the arrival time defined according to the criteria above is too late. Further, the dominance of low frequencies at large offsets may result in an offset-dependant bias. Therefore, we calibrate the models with record travel times.

Compared to traditional tomographic inversion methods, models derived by the stacking technique exhibit lower resolution and accuracy due to smearing effects. The uniform grid size may lead to underestimation of the resolution in areas of high coverage. This can affect layers where local velocity variations are most pronounced, for example in the sedimentary basins. The robustness of the method ensures that the velocity error in the uppermost layers are not projected into deeper layers, but results in a higher travel time residual and thereby lower accuracy.

It has been demonstrated that the 1-D inversion of arrival times picked from CMP-sorted and stacked *Pg* phases is highly independent from the starting model, but also that it may provide smeared models in case of a low velocity or low gradient zone (Appendix C). Due to the constraints inherent in the 1-D inversion, overall the middle crust is better constrained by $v^s{}_{Pg}$ than by models derived by 3-D tomography. The inversion method applied to *Pn* stacks is a back-projection technique and it converges for the present data set.

In our case the vertical gradient of the uppermost mantle velocity cannot be derived from the data. Delay times, laterally variable velocities and laterally variable vertical velocity gradients cannot be determined simultaneously. Therefore, gradients may be only estimated from interactive amplitude modelling. However, in our case we had to assume a small constant vertical velocity gradient in order to increase the coherency of the *Pn* arrivals prior to stacking.

Stacking *Pn* and *PmP* arrivals provides the basis for construction of Moho depth models in the time domain. We consider this as an advantage due to the lack of information on velocity in the lower crust. The data is acquired in time and any conversion to depth involves a model of velocity, which introduces additional uncertainty. For data from WAR/R experiments, perhaps only 20 percent – 50 percent of the crust is covered by *Pg* diving waves. V_{nmo} velocities derived from stacked *PmP* waves should constrain the velocity of the lower crust to some extent. However, the assumptions inherent in the CMP-processing of wide-angle data reduce the accuracy of the obtainable velocity information, especially in areas of strongly varying crustal structure. Therefore we only obtain velocity information on the lower crust from 2-D interactive modelling by ray tracing. The representation of the Moho depth in the time domain offers a sound solution for later integration of improved velocity models of the crust.

7.2 The seismic models

The surface geology largely corresponds to the uppermost depth slices through the velocity model v_{Pg} (Fig. 17). The most prominent near surface structures of the velocity model v_{Pg} are the Pannonian, Vienna and Molasse Basins with velocities $<4500\ \mathrm{m\,s^{-1}}$. The Mid-Hungarian Range can be clearly identified as an area of high velocity within the Pannonian Basin. The velocities of the crystalline basement in the upper crust (<10 km) range from 5500 – $6300\ \mathrm{m\,s^{-1}}$. Areas of relatively low velocities within the upper crust of the Bohemian Massif are the Eger Graben and the granitic intrusions of the Moldanubian and the Tauern Window. A W-E striking belt of relatively high velocities north of the Tauern Window correlates with Paleozoic crystalline rocks near the sinistral strike-slip fault (SEMP-line). High velocities are also found in the External Dinarides and the Adriatic foreland (peninsula Istria), what has also been reported from earlier investigations (Carulli *et al.* 1990).

The seismic velocities at mid-crustal levels (10–20 km) range between $5900\ \mathrm{m\,s^{-1}}$ and $6400\ \mathrm{m\,s^{-1}}$. Relatively low velocities exist beneath the Molasse basin and the granitic intrusions of the Moldanubian. The Mid-Hungarian line separates low velocities in the north-west from high velocities in the south-east. The previously mentioned W-E striking high velocity zone north near the SEMP-line penetrates from the upper crust to the middle crust. The most significant velocity structure of the lower crust (>20 km) is an extended area of high velocities ($>7000\ \mathrm{m\,s^{-1}}$) in the northwestern Pannonian Domain.

Anisotropy has not been included in the presented methods. The deep-seated high velocity anomaly north of the Tauern Window may not be solely explained by the presence of palaeozoic rocks. For the Tauern Window itself, up to 10 percent of anisotropy has been interpreted from previous investigations with the fast axis aligned in W-E direction (Bleibinhaus & Gebrande, 2006). However, the analysis by Behm (2006) shows that this high velocity region is mainly covered by rays with N-S-direction in $v^s{}_{Pg}$. The azimuthal distribution of rays travelling through the high velocity lower crust in the northwestern Pannonian Domain is homogenously such that there is no significant preferred direction of the rays contributing to the *Pg* stacks.

The long wavelength Moho topography (Fig. 21) corresponds largely to the European Moho map of the investigation area (Dèzes & Ziegler 2001). However, our results reveal significant local anomalies. The depth to the Moho in the study area varies between 24 km (Eastern Croatia, Southern Slovakia) and 51 km (Alpine root). Our new results suggest a deeper Moho at the Alpine root (3 to 6 km deeper than in previous models) and beneath the Alpine foreland (1 to 3 km). A shallower Moho than shown by Dèzes & Ziegler (2002) is found in the areas of the Czech Republic, Slovakia, Slovenia and Eastern Croatia (differences of 0.5 to 2 km). The local Moho depression in Hungary correlates with the location of the Mid-Hungarian mountain range.

The Moho depths depend to some degree on the velocity model for the lower crust. The velocity estimates for the lower crust are generally undetermined, such that also the exact depth to Moho is subject to some uncertainty, whereas the relative changes in Moho depth probably are better constrained. The determination of fragmentation of the Moho is robust to any possible variation in lower crustal velocity, and it may be the most important outcome of this study. Results from previous and new 2-D interpretations (Yan & Mechie, 1989; Scarascini & Cassinis, 1997; Lüschen *et al.* 2004; Bleibinhaus & Gebrande, 2006) are in agreement with the concept of three Moho parts in the area of the Eastern Alps.

8 CONCLUSIONS

Stacking and inversion techniques have been applied to data from recent 3-D WAR/R projects. In comparison with traditional inversion methods based on travel time picks from record sections, we obtain a better coverage of the velocity models. Depth and velocity information has been obtained in regions where record travel time picking is unreliable due to low S/N-ratio. However, the inherent data simplification leads to models with lower resolution than interpretations based on phase picking in record sections, in particular for the uppermost layers. A systematic bias of the picked travel times from stacked data has been calibrated with travel times from record sections.

We have shown that, in areas with matching coverage, stacking and traditional travel time tomography result in similar large-scale structures. Therefore, the *combination of both methods* offers several benefits:

(i) The reliability is high, since models derived by the stacking techniques are based on robust travel time picks.

(ii) The robust models from stacking can be used as improved initial models for 3-D travel time tomography based on record travel times, since they are near to the global optimum solution.

(iii) Travel time information is preserved where it is available.

Stacking of WAR/R data is useful in cases with a low S/N ratio and significant 3-D geometrical features. Further research should be dedicated to synthetic tests addressing the resolution power of the stacking methods.

Zones of high and low velocities have been identified in the crust, which can be related to tectonic units. We have identified three characteristic crustal blocks in the Eastern Alps with significantly different depths to the Moho. The presented 3-D model forms a strong basis for an integrated tectonic interpretation of detailed 2-D velocity models from the area.

ACKNOWLEDGMENTS

We thank Regina Lippitsch and several anonymous reviewers whose thoughtful remarks not only greatly improved the manuscript, but also clarified several issues of the new methods for ourselves. Fruitful discussions with the members of the CELEBRATION 2000 and ALP 2002 working groups also contributed to the successful development of the stacking methods. Major parts of this study were funded by the Austrian Science Fund (FWF project P15576).

REFERENCES

Alpine Explosion Seismology Group, Reporter H.Miller, 1976. A lithospheric seismic profile along the axis of the alps, 1975: I: First results. *Pure Appl. Geophys.,* **114,** 1109–1130.

Astiz, L., Earle, P. & Shearer, P., 1996. Global stacking of broadband seismograms. *Seismol. Res. Lett.,* **67**(4), 8–18.

Behm, M., 2006. Accuracy and resolution of a 3D seismic model of the Eastern Alps. *Ph.D. thesis*, Vienna University of Technology, Vienna.

Beranek, B. & Zounkova, M., 1979. Principal results of deep seismic soundings, in: *Geodynamic Investigations Czechoslovakia*, final report, Veda, Slovak Ak. Of Science, Bratislava, pp. 105–111.

Bleibinhaus, F. & Gebrande, H., 2006 Crustal structure in the Eastern Alps along the TRANSALP profile from wide-angle seismic tomography. *Tectonophysics,* **414,** 51–69.

Brückl, E. *et al.* ALP 2002. Working Group, 2003. ALP 2002 Seismic Experiment, *Stud. Geoph. Geod.,* **47,** 671–679.

Carulli, G.B., Nicolich, R., Rebez, A. & Slejko, D., 1990. Seismotectonics of the NW external dinarides. *Tectonophysics,* **179,** 11–25.

CELEBRATION & ALP 2002 Working groups, 2004. Internal report of the ALP 2002 meeting, Vienna, February 2004. Institute of Geodesy and Geophysics, Vienna University of Technology.

Červený, V. & Psencik, I., 1984. Documentation of Earthquake Algorithms. SEIS83 – Numerical modeling of seismic wave fields in 2-D laterally varying layered structures by the ray method. E.R.Engdahl edit., Report SE-35, Boulder, pp. 36–40.

Claerbout, J., 1985. *Imaging the Earth's Interior*, Blackwell Scientific Publications, Oxford.

Christensen, N. & Mooney, W., 1995. Seismic velocity structure and composition of the continental crust: a global view, *J. Geophys. Res.,* **100**(B7), 9761–9788.

Dèzes, P. & Ziegler, P.A., 2001. European Map of the Mohorovicic discontinuity. 2nd EUCOR-URGENT Workshop (Upper Rhine Graben Evolution and Neotectonics), Mt. St. Odile, France.

Doglioni, C. & Bosselini, A., 1987. Eoalpine and mesoalpine tectonics in the Southern Alps. *Geologische Rundschau.* **76**(3), 735–754.

Dragašević, T., Andrić, B. & Joksović, P., 1990. *Yugoslavia Structural map of Mohorovičić discontinuity 1:500 000 with Explanation*. Federal Geological Survey, Beograd.

The ECORS-CROP Deep Seismic Sounding Group:Hirn, A. *et al.*, 1989. Mapping the Moho of the Western Alps by wide-angle reflection seismics, *Tectonophysics,* **162,** 193–202.

Faust, L.Y., 1951. Seismic velocity as a function of depth and geologic time. *Geophysics,* **16,** 192–206.

Gardner, L.W., 1939. An areal plan for mapping subsurface structure by refraction shooting. *Geophysics,* **4,** 247–259.

Giese, P., 1976. *Explosion Seismology in Central Europe*, eds P. Giese, C. Prodehl & A. Stein, Springer Verlag Berlin, Heidelberg, New York.

Grassl, H., Neubauer F., Millhan K. & Weber F., 2004. Seismic image of the deep crust at the eastern margin of the Alps (Austria): indications for crustal extension in a convergent origin, *Tectonophysics,* **380,** 105–122.

Guterch, A., Grad, M. & Keller, G.R., 2001. Seismologists celebrate the new millenium with an experiment in Central Europe. *EOS, Trans. AGU,* **82**(529), 534–535.

Guterch, A., Grad, M., Špičák, A., Brueckl, E., Hegedus, E., Keller, G.R., Thybo, H. & CELEBRATION, 2000, ALP 2002, SUDETES 2003 Working Groups, 2003a. An overview of recent seismic refraction experiments in Central Eurupe, *Stud. Geoph. Geod.,* **47,** 651–657.

Guterch, A., Grad, M., Keller, G.R., Posgay, K., Vozar, J., Špičák, A., Brückl, E., Hajnal, Z., Thybo, H., Selvi, O. & CELEBRATION 2000 Experiment Team, 2003b: CELEBRATION 2000 Seismic Experiment, *Stud. Geoph. Geod.*, **47**, 659–669.

Hajnal, Z. *et al.*, 1996. Crustal-scale extension in the central Pannonian basin, *Tectonophysics* **264,** 191–204.

Hole, J.A., 1992. Nonlinear high-resolution three-dimensional seismic travel time tomography. *J. Geophys. Res.,* **97,** 6553–6562.

Hobro, J.W.D, Singh, S.C. & Minshull, T.A., 2003. Three-dimensional tomographic inversion of combined reflection and refraction seismic data. *Geophys. J. Intl.,* **152,** 79–93.

Hrubcová, P., Sroda, P., Špičák, A., Guterch, A., Grad, M., Keller, R., Brueckl, E. & Thybo, H., 2005. Crustal and uppermost mantle structure of the Bohemian Massif based on data from CELEBRATION 2000 Experiment, *J. Geophys. Res.,* doi:10.1029/2004JB003080.

Iwasaki, T., 2002. Extended time-term method for identifying lateral structural variations from seismic refraction data. *Earth Planets Space,* **54,** 663–677.

Joksović, P. & Andrić, B., 1983. *Report on Examination of Earth Crust Composition by Deep Seismic Sounding on the Profile of Pula – Maribor*. Expert Document Fund, Geofizika, Zagreb.

Kirchheimer, F., 1988. A tomographic approach to 3D refraction statics. 5th Annual Meeting of the European Association of Exploration Geophysicists, Proceedings, The Hague, Netherlands.

Lüschen, E., Lammerer, B., Gebrande, H., Millahn, K., Nicolich, R. & TRANSALP Working Group, 2004. Orogenic structure of the Eastern Alps, Europe, from TRANSALP deep seismic reflection profiling, *Tectonophysics,* **388,** 85–102.

Mayerova, M., Novotny M. & Fejfar, M., 1994. Deep seismic sounding in czechoslovakia, in *Crustal structure of the Bohemain Massif and the West Carpathians*. ed. Bucha, V., Blizkovsky, M., Praha, Academia.

Posgay, K. *et al.* 1996. International deep reflection survey along the Hungarian Geotraverse, *Geoph. Trans.* **40**(1–2), 1–44.

Psencik, I., 1998. Package ANRAY, version 4.10. in: *Seismic Waves in Complex 3-D Structures*, Report 7, pp. 403–404, Department of Geophysics, Charles University Prague. Available on: http://sw3d.mff.cuni.cz.

Ratschbacher, L. *et al.*, 1991. Lateral Extrusion in the Eastern Alps, *Tectonics,* **10,** 245–271.

Richards-Dinger, K.B. & Shearer P.M., 1997. Estimating crustal thickness in southern California by stacking PmP arrivals, *J. Geophys. Res.,* **102,** 15211–15224.

Skoko, D., Prelogovic, E. & Aljinovic, B., 1987. Geological structure of the Earth's crust above the Moho discontinuity in Yugoslavia, *Geophys. J. Royal Astronom. Soc.,* **89,** 379–382.

Scarascia, S. & Cassinis, R., 1997. Crustal Structures in the central-eastern Alpine sector: a revision of the availaible DSS data. *Tectonophysics,* **271,** 157–188.

Schmid, S., Fügenschuh, B., Kissling, E. & Schuster, R., 2004. Tectonic map and overall architecture of the Alpine orogen. *Swiss J. Geosci.,* **97**(1), 93–117.

Sheriff, R.E. & Geldart, L.P., 1995. *Exploration Seismology*, 2nd edn., Cambridge University Press, p. 592.

Song, L.-P., Koch, M., Koch, K. & Schlittenhardt, J., 2004. 2-D anisotropic Pn-velocity tomography underneath Germany using regional traveltimes. *Geophys. J. Intl.,* **157,** 645–663.

Tarantola, A., 1987. *Inverse Problem Theory*. Elsevier Scientific Publishing Company, New York.

Telford, W.M. *et al.*, 1990. *Applied Geophysics*, 2nd edn., Cambridge University Press, Cambridge.

Tomek, C., 1993. Deep crustal structure beneath the Central and inner West Carpathians, *Tectonophysics.,* **226,** 417–431.

Tomljenovic, B. & Csontos, L., 2001. Neogene-Quaternary structures in the border zone between Alps, Dinarides and Pannonian basin (Hrvatsko Zagorje and Karlovac basins, Croatia). *Int. J. Earth Sci.,* **90,** 560–578.

Toomey, D.R., Solomon, S.C. & Purdy, G.M., 1994. Tomographic imaging of the shallow crustal structure of the East Pacific Rise at 9°30′N. *J. Geophys. Res.,* **99,** 24135–24157.

Valasek, P., Mueller, St., Frei, W. & Holliger, K., 1991. Results of NFP 20 seismic reflection profiling along the Alpine section of the European Geotraverse (EGT). *Geophys. J. Intl.,* **105,** 85–102.

Vidale, J.E., 1990. Finite-difference calculation of travel times in three dimensions. *Geophysics,* **55,** 521–526.

Yan, Q.Z. & Mechie, J., 1989. A fine section through the crust and lower lithosphere along the axial region of the Alps. *Geophys. J. Intl.,* **98,** 465–488.

Yilmaz, Ö., 2001. *Seismic data analysis*, 2nd edn. Society of Exploration Geophysicists, Tulsa.

Zelt, C. A. & Smith, R.B., 1992. Seismic travel time inversion for 2-D crustal velocity structure, *Geophys. J. Intl.,* **108,** 16–34.

Zelt, C.A, 1998. Lateral velocity resolution from 3-D seismic refraction data. *Geophys. J. Intl.,* **135,** 1101–1120.

Zelt, C.A. & Barton, P.J, 1998. Three-dimensional seismic refraction tomography: A comparision of two methods applied to data from the Faero Basin. *J. Geophys. Res.,* **103**, 7187–7210.

Zelt, C.A., Hohjka, A.M., Flueh, E.R. & McIntosh, K.D, 1999. 3D simultaneous seismic refraction and reflection tomography of wide-angle data from the central Chilean margin. *Geophys. Res. Lett.,* **26,** 2577–2580.

APPENDIX A: GLOSSARY OF USED MODELS AND NONSTANDARD ABBREVIATIONS

Models with their names written in bold letters are considered to be final and are used for interpretation.

Model/Abbreviation	Description
SRC	Source
RCV	Receiver
l_G	Grid spacing
l_C	Cell size
l_B	Bin size
OFB	Offset bin
$v^s{}_{Pg}(x,y,z)$	Crustal velocity model derived from stacked *Pg* phases
$v^{1D}{}_{Pg}(z)$	Crustal velocity model derived from averaging $v^s{}_{Pg}(x,y,z)$
$v^{T1}{}_{Pg}(x,y,z)$	Crustal velocity model derived from tomographic inversion of *Pg* travel times using $v^{1D}{}_{Pg}(z)$ as initial model
$v^{T3}{}_{Pg}(x,y,z)$	Crustal velocity model derived from tomographic inversion of *Pg* travel times using $v^s{}_{Pg}(x,y,z)$ as initial model
$R(x,y,z)$	Resolvability parameters (Zelt 1998) calculated for $v^{T3}{}_{Pg}(x,y,z)$
$v_{Pg}(x,y,z)$	Final crustal velocity model derived from merging $v^s{}_{Pg}(x,y,z)$ and $v^{T3}{}_{Pg}(x,y,z)$
$v^s{}_{Pn}(x,y)$	Uppermost mantle velocity model derived from stacked *Pn* phases
$td^s(x,y)$	Moho delay time model derived from stacked *Pn* phases
$v^{T1}{}_{Pn}(x,y)$	Uppermost mantle velocity model derived from delay time inversion of *Pn* travel times using a constant initial delay time & constant initial velocity
$td^{T1}(x,y)$	Moho delay time model derived from delay time inversion of *Pn* travel times using a constant initial delay time & constant initial velocity
$td^{T3}(x,y)$	Moho delay time model derived from delay time inversion of *Pn* travel times using $td^s{}_{Pn}(x,y)$ and $v^s{}_{Pn}(x,y)$ as initial models
$\Delta td^{T3}(x,y)$	Difference between $td^{T3}(x,y)$ and $v^s{}_{Pn}(x,y)$ (delay time improvements)
$r(x,y)$	Resolution elements of $\Delta td^{T3}(x,y)$
$f(x,y)$	Damping factor calculated from $r(x,y)$ for the combination of $td^{T3}(x,y)$ and $td^s(x,y)$
$td(x,y)$	Final Moho delay time model derived from merging $td^s(x,y)$ and $td^{T3}(x,y)$
$V_{nmo}(x,y)$	Velocity model for NMO correction derived from *PmP* phases
$T0^s(x,y)$	Unmigrated two way normal incidence times of the Moho derived from stacked *PmP* phases
$Z_M(x,y)$	Approximate Moho depth-model from depth-conversion of $td(x,y)$ with $v_{Pg}(x,y,z)$ and $v^s{}_{Pn}(x,y)$
$\bar{s}(x,y)$	Mean slowness between Z = 10 km and $Z_M(x,y)$
$\bar{q}(x,y)$	Mean vertical slowness-component for a ray critically refracted from the Moho
$T0^d(x,y)$	Unmigrated two way normal incidence times of the Moho derived from transforming $td(x,y)$
$T0(x,y)$	Unmigrated two way normal incidence times of the Moho derived from merging $T0^s(x,y)$ and $T0^d(x,y)$
$T0_{mig}(x,y)$	Migrated two way normal incidence times of the Moho derived from $T0(x,y)$ from which the absolute Moho depths are calculated

APPENDIX B: STATIC CORRECTIONS ACCOUNTING FOR NEAR SURFACE STRUCTURES

The static corrections are derived from an extrapolated delay time model (Fig. B1) of the sedimentary layer. This delay time model is calculated from *Pg* travel time picks (Fig. 2a) in the offset range of 25–80 km.

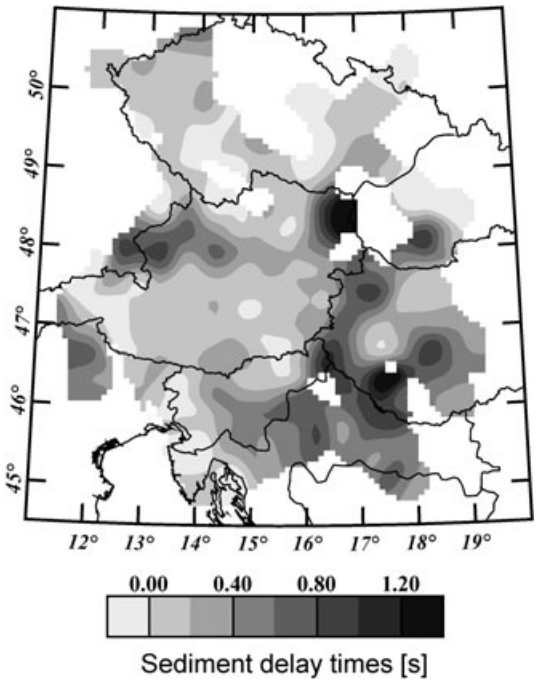

Figure B1. Delay time model of the sedimentary layer (used for static corrections).

APPENDIX C: RAY TRACING & INVERSION FOR 1-D MEDIA

We consider a sequence of layers with constant vertical velocity gradients k. Each layer is limited by an upper boundary at $z = z_u$ and a lower boundary at $z = z_l$. The slowness at the upper boundary is s_u and at the lower boundary is s_l.

The ray geometry is determined by the ray parameter p and an approximation $v_0(z) = s_0(z)^{-1}$ of the velocity field $v(z)$. From the following basic relations

$$dx = \frac{v(z) \cdot p}{\sqrt{1 - (p \cdot v_0(z))^2}} \cdot dz \tag{C1}$$

$$dt = \frac{1}{v(z)} \cdot dl = \frac{1}{v(z)} \cdot \frac{1}{\sqrt{1 - (p \cdot v_0(z))^2}} \cdot dz \tag{C2}$$

we find by integration

$$\Delta x = \frac{1}{k \cdot p} \cdot \left(\sqrt{1 - \eta_u^2} - \sqrt{1 - \eta_l^2}\right) \tag{C3}$$

$$\Delta t = \frac{1}{k} \cdot \left(\operatorname{acosh}\left(\frac{1}{\eta_u}\right) - \operatorname{acosh}\left(\frac{1}{\eta_l}\right)\right) \tag{C4}$$

with

$$k = \frac{1}{s_u \cdot s_l} \cdot \frac{s_u - s_l}{z_l - z_u} \tag{C5}$$

$$\eta_u = \frac{p}{s_u} \tag{C6}$$

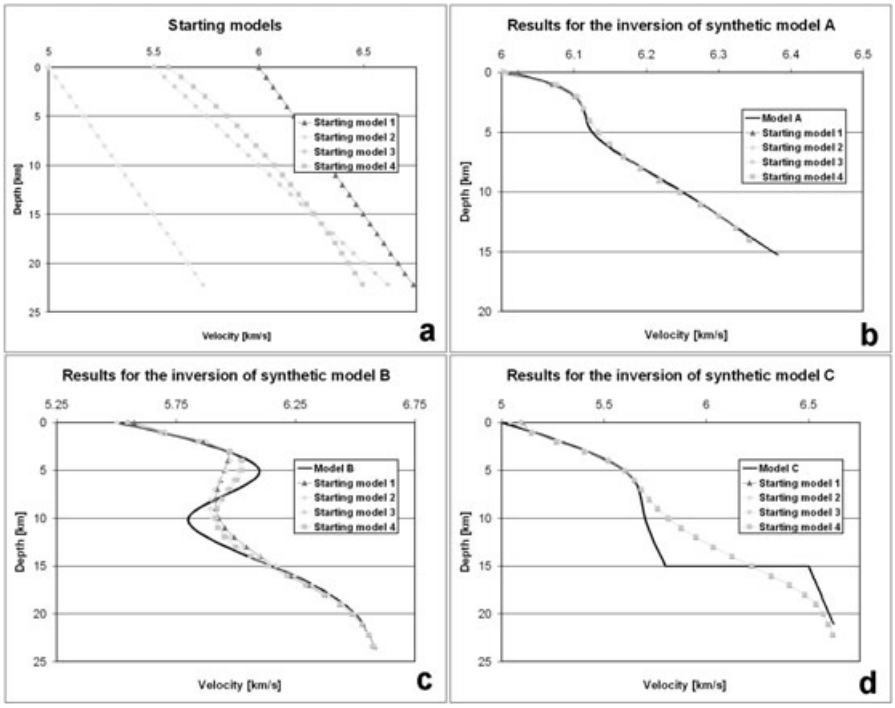

Figure C1. 1-D Inversion of synthetic travel times. For three synthetic models A, B, C (black solid lines in figures b and c), travel times were calculated using the program ANRAY (Psencik, 1998). The number of travel times was chosen to be similar to real observations. These travel times were inverted using the same algorithm as for the real data. Four different starting models (fig a) were tested. The results are shown by the symbols connected by lines in the fig (b) and (c). There is almost no influence of the starting model. Velocity inversions and interfaces of first order can only be approximately reproduced.

$$\eta_l = \frac{p}{s_l} \tag{C7}$$

(C3) and (C4) describe the ray tracing equation for one layer in a 1-D medium. Δx is the horizontal offset the ray travels in the time Δt within a layer of thickness $z_l - z_u$ and the velocities $1/s_u$ and $1/s_l$.$s(z)$ is determined by inversion of matrix W

$$\Delta t = \mathbf{W}^{\mathbf{T}} \cdot \begin{pmatrix} s_u \\ s_l \end{pmatrix} \tag{C8}$$

By linear interpolation of the slowness instead of the velocity, we find

$$\mathbf{W} = \begin{pmatrix} \int_{z_u}^{z_l} \frac{z-z_u}{z_l-z_u} \cdot \frac{1}{\sqrt{1-\left(p\cdot\left(\frac{1}{s_u}+k\cdot(z-z_u)\right)\right)^2}} \cdot dz \\ \int_{z_u}^{z_l} \frac{z_l-z}{z_l-z_u} \cdot \frac{1}{\sqrt{1-\left(p\cdot\left(\frac{1}{s_u}+k\cdot(z-z_u)\right)\right)^2}} \cdot dz \end{pmatrix} = \begin{pmatrix} C_u \cdot A + B \\ C_l \cdot A - B \end{pmatrix} \tag{C9}$$

$$A = a\sin(\eta_u) - a\sin(\eta_l) \tag{C10}$$

$$B = \frac{\sqrt{1-\eta_u^2} - \sqrt{1-\eta_l^2}}{p^2 \cdot k^2 \cdot (z_u - z_l)} \tag{C11}$$

$$C_u = \frac{1 + k \cdot s_u \cdot (z_l - z_u)}{p \cdot s_u \cdot k^2 \cdot (z_u - z_l)} \tag{C12}$$

$$C_l = \frac{-1}{p \cdot s_u \cdot k^2 \cdot (z_u - z_l)} \tag{C13}$$

Solving for the velocity function $v(z)$

The inversion for a velocity function $v(z)$ from a 1-D travel time curve t_{obs} *(offs)* follows the procedure:

(1) Definition of a starting model $v_0(z)$ and transformation to the corresponding slownesses $s_0(z)$

(2) Calculation of the ray geometry and travel times t_{calc} *(offs)* by (C3) and (C4)

(3) Modelling of dt *(offs)* $= t_{obs} - t_{calc}$ by corrections ds *(z)* of the parameters $s(z)$ by (C8).

(4) Addition of conditions to achieve a smooth solution and, in case of a velocity inversion, a stable one.

(5) Inversion for $ds(z)$ by applying Truncated Singular Value Decomposition (TSVD; e.g. Nolet, 1987) to the matrix W

(6) Improvement of the model $s(z)$ by addition of $ds(z)$ and iteration from step 2 until convergence is achieved

Tests show that stable solutions are found when a damping strategy is used. In each iteration step, the slowness improvement ds *(z)* is multiplied by a factor λ between 0.005 and 0.2. After 50–200 iteration steps a final solution $s(z)$ is obtained and converted to v *(z)*. The equation system is small (typical values are about 20 rows $\times$ 20 columns).

For all cells, the following starting model is used:

$$v_0(z) = 5000ms^{-1} + 0.033s^{-1} \cdot z \tag{C14}$$

This choice is relatively arbitrary since the influence of the starting model is insignificant (Fig. C1).

APPENDIX D: SURVEY SINKING

Refracted waves (*Pn*)

When a ray is specified by its ray parameter p, the ray can be traced to any depth according to eqs. (D3) and (D4). The ray is traced

from the surface points (source and receiver) to the reference datum (piercing points). The ray parameter p is calculated by differentiation of eq. (1). Downward continuation is performed under three simplifications: (1) The ray path is in a vertical plane through source and receiver; (2) The velocity field of the crust along the ray path from the surface to the new reference datum is represented by the velocity-depth function at the receiver location; and (3) The refractor velocity at the piercing point is substituted by the refractor velocity v_{Pn} at the receiver location. Under these premisses, the ray parameter $p(x,y,\alpha)$ for a ray at the receiver location (x,y) and with the back azimuth α from receiver to source follows from differentiation of eq. (1):

$$p = \frac{1}{v_{CPn}(x,y)} - \begin{pmatrix} \frac{d}{dx} td(x,y) \\ \frac{d}{dy} td(x,y) \end{pmatrix}^T \cdot \begin{pmatrix} \sin(\alpha) \\ \cos(\alpha) \end{pmatrix} \quad \text{(D1)}$$

Survey sinking of the source location applies the principle of reciprocity. The ray parameter according to eq. (D1) is based on *Pn* velocities $v_{Pn}(x,y)$ and delay times $td(x,y)$ at the surface level. In our case, these were calculated by the stacking technique as it is described in the text. However, the velocities and delay times needed for (D1) could also be obtained from any previous Moho models.

Reflected waves (*PmP*)

The ray parameter is calculated using eq. (D2) with $Z_{Moho} = 33$ km and $V_{nmo} = 6450$ m s^{-1} below Z = 10 km:

$$p = \frac{d}{d_{offset}} T_{PmP} = \frac{d}{d_{offset}} \sqrt{\left(\frac{2 \cdot Z_{Moho}}{V_{nmo}}\right)^2 + \left(\frac{Offset}{V_{nmo}}\right)^2} = \frac{1}{\sqrt{4 \cdot Z_{Moho}^2 + Offset^2}} \cdot \frac{Offset}{V_{nmo}} \quad \text{(D2)}$$

Using these values, the effect of survey sinking is optimized for stacking of *PmP*-waves. Similar simplifications as for *Pn* waves are introduced.

APPENDIX E: TRACE FOLD OF STACKED DATA

Trace fold

The trace fold is an important quality criterion for stacked data. Although it is assigned to the bins, we show the average trace fold over all bins for each cell in case of OFB-stacks (Figs E1 and E2). For the CMP- and SRC&RCV-stacks, the bin is identical to the cell (Figs E3 and E4).

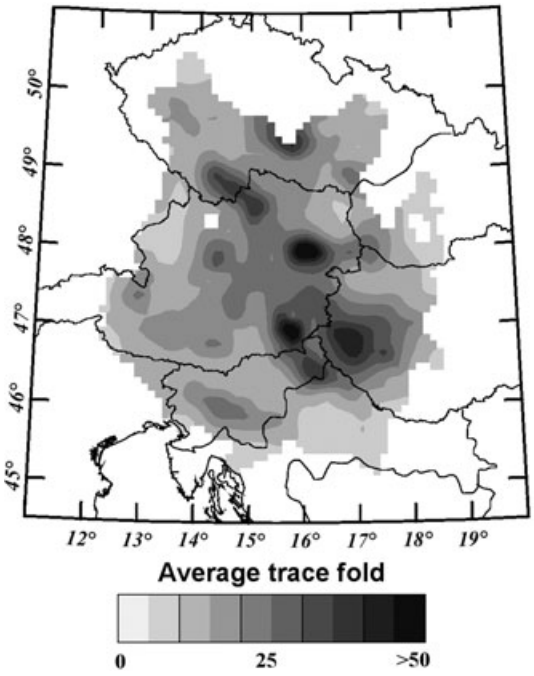

Figure E1. Average trace fold over all offset bins for OFB-stacks of *Pg* waves.

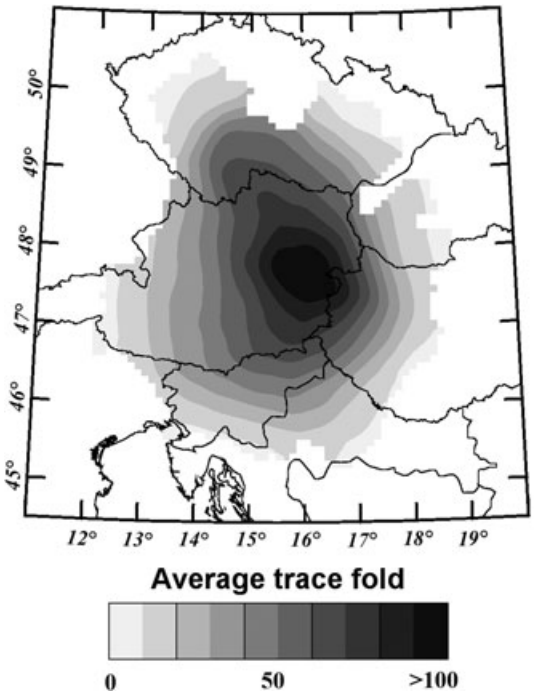

Figure E2. Average trace fold over all offset bins for OFB-stacks of *Pn* waves.

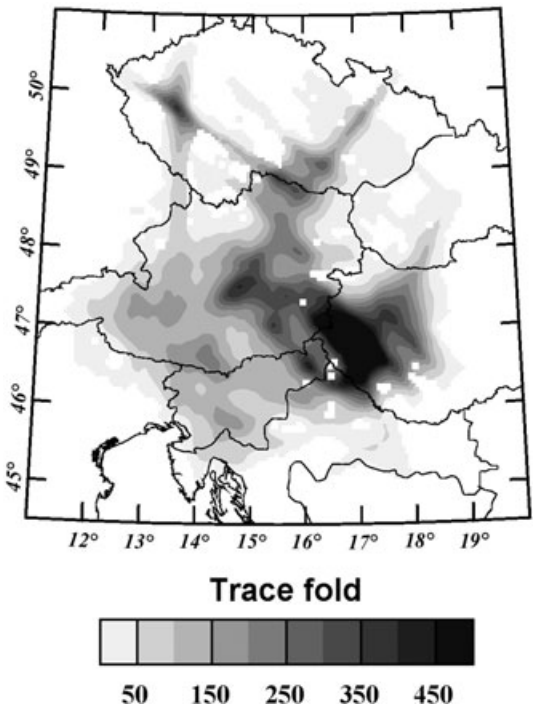

Figure E3. Trace fold for CMP-stacks of *PmP* waves.

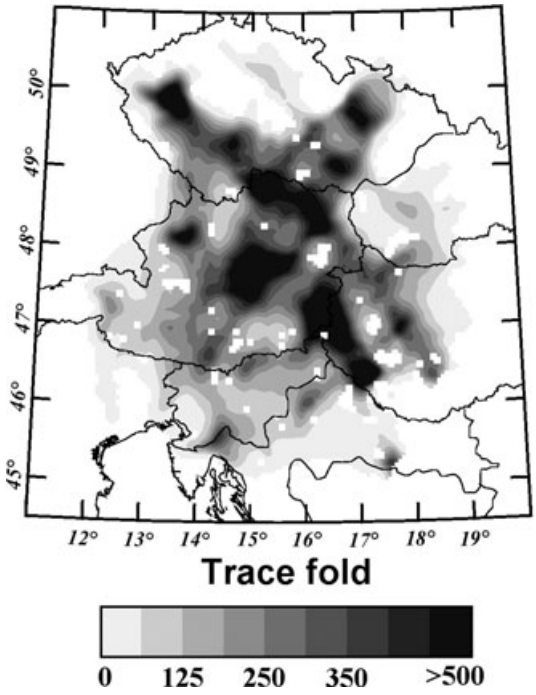

Figure E4. Trace fold for SRC&RCV-stacks of *Pn* waves.